Université catholique de Louvain

École polytechnique de Louvain (EPL)

Radiation Pattern of the SKALA antenna in the vicinity of a finite ground plane

Dissertation presented by
Jean Cavillot

for obtaining the Master's degree in
Electrical Engineering

Supervisor
Christophe Craeye

Readers
Ha Bui Van, Eloy de Lera Acedo,Claude Oestges,François Glineur

Academic year 2016-2017

Thanks,

I would first thank those who helped me throughout the achievement of this Master Thesis.

I would particularly thank Professor Christophe Craeye for his advices and guidance.

I am also greatly thankful for the help and the implication of Ha Bui Van during this project.

Finally, I thank Hardie Pienaar and Dr Eloy de Lera Acedo for the FEKO simulations that allowed me to validate my results.

Abstract

One of the challenges regarding the SKA radio-telescope is the determination of the radiation pattern of the low frequency antenna in presence of a finite ground plane. In this Master Thesis, a methodology based on a spectral approach is built to calculate relatively fast the current induced in a finite ground plane placed under a given source. The field radiated by the source is estimated thanks to a method based on the decomposition into inhomogeneous plane waves and the current induced in the ground plane is calculated by solving a Method of Moments linear system of equations. The method is applied to the low frequency antenna of the SKA for different frequencies and ground plane diameters. The results are validated against the ones obtained with the EM simulation software FEKO.

Contents

Glossary

A_n^-	Area of the triangle carrying a decaying edge basis function
A_n^+	Area of the triangle carrying a rising edge basis function
$\hat{e}$	TM polarization vector
ϵ	Permittivity
E_p	Electric field for polarization p
η	Free space impedance
f	Frequency
F_p	Radiation Pattern for polarization p
Γ	Reflection coefficient
HARP	Harmonic-polynomials
k	The wavenumber
$\overrightarrow{k}$	Direction of polarization
λ	The wavelength
LFAA	Low Frequency Aperture Array
MFAA	Mid Frequency Aperture Array
$\hat{m}$	TE polarization vector
μ	Permeability
N_{bf}	Number of basis functions on the antenna
N_{tf}	Number of testing functions on the ground plane
ϕ	Azimuth angle
SDP	Steepest Descent Path
SKA	Square Kilometer Array
SKALA	SKA Log-periodic Antenna
θ	Elevation angle
v	Excitation vector on the ground plane

Chapter 1

Introduction: The SKA

The Square Kilometer Array (SKA) [1], [2] is the next generation of radio telescope. Its target sensibility aims to be significantly higher than any other current telescope and its long term goal is to bring answers to important questions like:

- What did the universe look like when the first galaxies formed ?
- What are gravitational waves ?
- How are planets formed ?
- What is dark matter ?

The desired high sensitivity requires a huge number of elements and a significantly large collecting area to be able to overcome the sky brightness temperature. The full SKA will contain more than 3 million elements and the implementation is currently taking place in South Africa and in Australia. The construction sites are remote areas chosen far away from cities to benefit from a minimum radio interference. The total collecting area of the SKA will be over one square kilometer.

The SKA will be built in two phases. The first one takes place between 2017 and 2023 and is about procurement and construction. The needed sensitivity for the first phase requires already about 250,000 elements. The second phase should end during the 2020s.

The use of so many elements means a high signal processing capability. The central signal processor needs to convert signals from the receivers to valid information like images of deep space astronomical phenomena. The central signal processor will use the latest generation of high-speed processors and high capacity memory chips.

Apart from the technological part is the need for a low design cost of the elements. The design approach is limited by the price of such a huge number of elements. Moreover, the SKA is specified to be operative for at least 30 years which means a high reliability of the elements.

The targeted goals of the SKA require a high frequency bandwidth of the installation. The receivers must cover a frequency bandwidth from 50 MHz to 10 GHz. Scanning all these frequencies means different receiver implementations.

The SKA receivers

The SKA is equipped with three types of receivers covering different frequency bands. These receivers are described below:

1) The Low Frequency Aperture Array (LFAA)

The LFAA is made of stationary antennas, board amplifiers and local processing elements. It also requires a local signal processing station to combine the antennas. This implementation is the so-called low-SKA and will cover the frequency band from 50 MHz to 350 MHz.

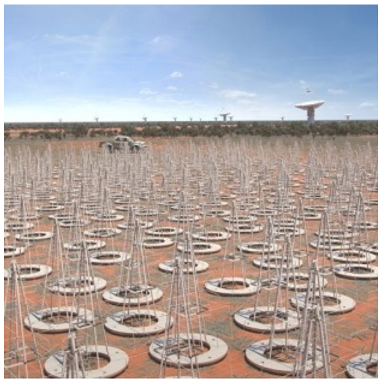

Figure 1.1: Low Frequency Aperture Array in Australia. Reference: [1].

2) The Mid Frequency Aperture Array (MFAA)

The MFAA will cover the frequencies from 450 MHz to 1500 MHz. This aperture will be deployed in the second phase of the SKA construction.

The MFAA will have specific planned missions such as measuring the effects of dark energy. It needs to detect very small signal variations and then requires a significantly high sensitivity.

Figure 1.2: Mid Frequency Aperture Array in South Africa. Reference: [1].

3) The High Frequency Network

A combination of several thousands of 15 meters wide dishes gives the telescope its high frequency capability (from 1500 MHZ to 10 GHz). This network of dishes will be used as an interferometer.

In contrast with the LFAA and the MFAA, these antennas will be steerable. The dishes will be composed of carbon fiber composites and will be able to resist high winds and environmental stresses.

Figure 1.3: The 15 meter wide dish. Reference: [1].

The low-SKA

In this master thesis we will focus on the elements of the Low Frequency Aperture Array. The design of the LFAA antenna has been quite challenging due to the many requirements of the radio-telescope. Indeed it should be a dual-pol element with significant performance in terms of radiation patterns, low cross-polarization, impedance matching,... The proposed design is the SKALA (SKA Log-periodic Antenna) element and is pictured in Figure 1.4.

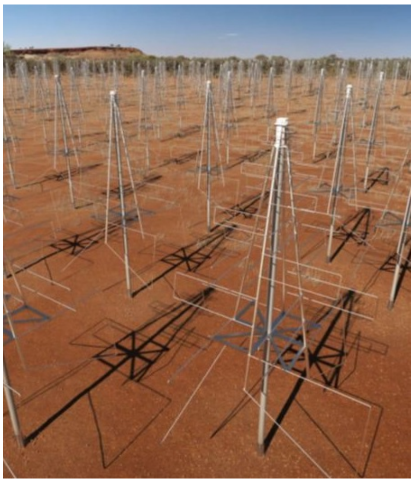

Figure 1.4: Artist's image of SKA-low array dipole antennas – Swinburne Astronomy Productions/ICRAR/U. Cambridge/ASTRON. Reference: [1].

The antenna has two orthogonal horizontally polarized V-shaped log-periodic elements. Due to dimensions constraints, the antenna has a maximum height of 1.5 m.

1.1 Context and goal of the Master Thesis

The latest requirements of the SKA stipulate that each of the low-SKA stations will contain 256 elements. The sensitivities of the array elements are different from each other due to mutual coupling. A software code named HARP [3], [17] developed at UCL measures efficiently the effect of mutual coupling taking into account an infinite ground plane.

In this Master Thesis, we want to estimate the radiation pattern of the antennas including the presence of a finite ground plane. The culmination of the project requires the following steps:

1. Find a way to compute the electric field radiated by the antenna on the finite ground plane.
2. Determine the current induced in the ground plane.
3. Compute the radiation pattern of the antenna in the vicinity of the finite ground plane.

The Master Thesis is organized as follows: the first chapters will introduce and describe the different methods used to compute the field incident to the ground plane and the current induced in this one. After that, the methodology will be applied and validated with several kinds of antennas and finally with the SKALA antenna.

More precisely, the Chapter 2 will explain how to compute the electric field radiated by a 3D antenna on a plane situated just below this one using a spectral approach. Advantages and disadvantages of the method will be discussed and a validation using dipoles will be described.

The Chapter 3 gives some notions about the Method of Moments and explains how it can be used to determine the current induced on the finite ground plane. The Chapter 4 is devoted to the computation of discrete integrals which will help us to solve the system of equations dictated by the application of the Method of Moments.

After that, the Chapter 5 will describe the validation of the method with different antennas. Finally, the method is applied to the SKALA antenna in Chapter 6.

Chapter 2

Estimation of the field radiated by a source on a finite ground plane

The first step towards the calculation of the induced current in the ground plane is the determination of the incident field. The challenge is to find a fast method capable of handling 3D antennas. The method proposed here is a spectral approach based on the decomposition into inhomogeneous plane waves [4].

This chapter will first give a background necessary to the understanding of the considered method. After that, the approximated radiated field using this approach is validated against its exact solution when considering small dipoles. The advantages and limitations of the spectral approach are then discussed.

Finally, the calculation of the reflection coefficients at a single interface is described.

2.1 Definitions

Let us consider a two semi-infinite medium environment as depicted in Figure 2.1.

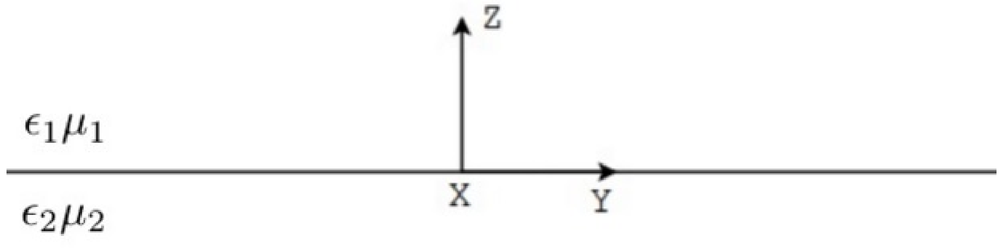

Figure 2.1: Coordinates in a two semi-infinite medium environment

The electromagnetic fields can be decomposed into TE and TM plane waves and can be expressed in each of the propagating media as:

$$\begin{aligned}\overrightarrow{E} &= (-\hat{m}\ A_{TE} + \hat{e}\ A_{TM})\, e^{-jk_x x} e^{-jk_y y} e^{\pm jk_z z} \\ \overrightarrow{H} &= \frac{1}{\eta_i}\,(\hat{e}\ A_{TE} + \hat{m}\ A_{TM})\, e^{-jk_x x} e^{-jk_y y} e^{\pm jk_z z}\end{aligned} \tag{2.1}$$

where $\eta_i = \sqrt{\frac{\mu_i}{\epsilon_i}}$ is the free space impedance of the medium i with permittivity ϵ_i and permeability μ_i, A_{TE} and A_{TM} are the complex amplitudes of the TE and TM plane waves and where the sign $\pm$ corresponds to a wave propagating in the $\mp z$ direction.

Each plane wave is characterized by its direction of propagation $\overrightarrow{k} = (k_x, k_y, \mp k_z)$. The norm of $\overrightarrow{k}$ is equal to the wavenumber k.

Considering $\beta \triangleq \sqrt{{k_x}^2 + {k_y}^2}$, k can also be expressed as:

$$k^2 = \beta^2 + k_z^2 \tag{2.2}$$

with

$$\mathbb{R}\{k_z\} \geq 0$$
$$\mathbb{I}\{k_z\} \leq 0.$$

The normalized direction of propagation $\hat{u}$ and the TE and TM polarization vectors $\hat{m}$ and $\hat{e}$ are defined as follows:

$$\hat{u} \triangleq \overrightarrow{k}/k, \tag{2.3}$$

$$\hat{m} \triangleq \frac{1}{\beta}\begin{bmatrix}-k_y \\ k_x \\ 0\end{bmatrix}, \tag{2.4}$$

$$\hat{e}^u \triangleq \frac{1}{\beta k}\begin{bmatrix}k_x k_y \\ k_y k_z \\ -\beta^2\end{bmatrix}, \tag{2.5}$$

for waves propagating in the $+z$ direction and

$$\hat{u} \triangleq \overrightarrow{k}/k, \tag{2.6}$$

$$\hat{m} \triangleq \frac{1}{\beta}\begin{bmatrix}-k_y \\ k_x \\ 0\end{bmatrix}, \tag{2.7}$$

$$\hat{e}^u \triangleq \frac{1}{\beta k}\begin{bmatrix}-k_x k_y \\ -k_y k_z \\ -\beta^2\end{bmatrix}, \tag{2.8}$$

for waves propagating in the $-z$ direction.

It can be noticed that the TE component characterized by $\hat{m}$ is always parallel to the boundary between the two media and that the polarization vectors $\hat{m}$, $\hat{e}$ and the direction of propagation $\hat{u}$ form an orthonormal basis:

$$\hat{u} = \hat{e} \times \hat{m}. \tag{2.9}$$

2.2 Electric Field on Ground

Starting from a current distribution situated above the finite ground plane given by $\overrightarrow{J}(\overrightarrow{r}')$, the potential vector $\overrightarrow{A}(\overrightarrow{r})$ reads:

$$\overrightarrow{A}(\overrightarrow{r}) = \int\int\int_V \overrightarrow{J}(\overrightarrow{r}')\ G(R)\ dV \tag{2.10}$$

where $\overrightarrow{r}'$ corresponds to the source point, $\overrightarrow{r}$ is the observation point and $R = |\overrightarrow{r} - \overrightarrow{r}'|$.

The Green function $G(R)$ can be expressed as the Weyl [5] integral as follows:

$$G(R) = \frac{e^{-jkR}}{4\pi R} = \frac{1}{(2\pi)^2} \int\int_{-\infty}^{+\infty} \frac{exp\left(-j\left(k_x(x-x') + k_y(y-y') + k_z|z-z'|\right)\right)}{2jk_z}\ dk_x\ dk_y. \tag{2.11}$$

In our context, we are mainly interested in the waves going in the $-z$ direction, thus $e^{-jk|z-z'|}$ can be rewritten $e^{jkz}e^{-jkz'}$.

From there, the electric field component with p polarization can be written as:

$$\begin{aligned}
E_p = \overrightarrow{E} \cdot \hat{e}_p &= -jk\eta(\overrightarrow{A} + \frac{\nabla(\nabla \cdot \overrightarrow{A})}{k^2}) \cdot \hat{e}_p \\
&= \frac{-jk\eta}{(2\pi)^2} \int\int_{(k_x,k_y)} \frac{exp\left(-j(k_x x + k_y y - k_z z)\right)}{2jk_z}\ \hat{e}_p \cdot \{I - \frac{\overrightarrow{k}\,\overrightarrow{k}}{k^2}\} \\
&\int\int\int_V \overrightarrow{J}(\overrightarrow{r}')\ exp\left(-j(k_x x' + k_y y' + k_z z')\right)\ dV\ dk_x\ dk_y
\end{aligned} \tag{2.12}$$

where I is the identity operator.

One may notice that the integration over spatial and spectral coordinates have been swapped. As the direction of propagation is orthogonal to each of the polarization directions, the term in $\frac{\overrightarrow{k}\,\overrightarrow{k}}{k^2}$ falls.

More generally, the field propagating in the $-z$ direction can be expressed as:

$$E_p(x, y, z) = \frac{-jk\eta}{(2\pi)^2} \int\int F_p(k_x, k_y)\ \frac{exp\left(-j(k_x x + k_y y - k_z z)\right)}{2jk_z}\ dk_x\ dk_y \tag{2.13}$$

where $F_p(k_x, k_y)$ is the radiation pattern of the considered current distribution for a polarization p.

The radiation pattern $F_p(k_x, k_y)$ is then given by:

$$F_p(k_x, k_y) = \int\int\int_V [\overrightarrow{J}(\overrightarrow{r}') \cdot \hat{e}_p]\ exp\left(-j(k_x x' + k_y y' + k_z z')\right) dV. \tag{2.14}$$

2.3 Contour deformation

Different contour deformations like the Steepest Descent Path (SDP) [4] [8] or the parabolic contour [6] have been adopted in the literature. As will be seen later, the appropriate contour deformation depends on the height of the current source with respect to the ground.

Let us first consider the SDP contour deformation. In this contour, the imaginary part of β is related to its real part by:

$$\beta_I = \frac{\beta_R}{S} \tag{2.15}$$

with $S = \sqrt{1 + \left(\frac{\beta_R}{k}\right)^2}$.

The complex wavenumbers $k_x = k_{xR} + jk_{xI}$ and $k_y = k_{yR} + jk_{yI}$ need to fulfill the following equations:

$$\beta^2 = k_x^2 + k_y^2, \tag{2.16}$$

$$\beta_R{}^2 = k_{xR}{}^2 + k_{yR}{}^2. \tag{2.17}$$

Knowing that $\beta^2 = \beta_R{}^2 + 2j\beta_R\beta_I - \beta_I{}^2$, the imaginary part $\beta_I{}^2$ can be found by subtracting (2.17) to the real part of (2.16), which produces:

$$\beta_I{}^2 = k_{xI}{}^2 + k_{yI}{}^2. \tag{2.18}$$

Taking the imaginary part of (2.16), we have:

$$\beta_R\beta_I = k_{xR}k_{xI} + k_{yR}k_{yI}. \tag{2.19}$$

Considering (2.18) and (2.19), we can write:

$$\beta_R{}^2\left(\frac{\beta_I}{\beta_R}\right)^2 = k_{xR}{}^2\left(\frac{k_{xI}}{k_{xR}}\right)^2 + k_{yR}{}^2\left(\frac{k_{yI}}{k_{yR}}\right)^2, \tag{2.20}$$

$$\beta_R{}^2\left(\frac{\beta_I}{\beta_R}\right) = k_{xR}{}^2\left(\frac{k_{xI}}{k_{xR}}\right) + k_{yR}{}^2\left(\frac{k_{yI}}{k_{yR}}\right). \tag{2.21}$$

by multiplication with ratios of type $\frac{\epsilon}{\epsilon}$ [6].

From equations (2.17), (2.20) and (2.21), the following equation can be inferred:

$$\frac{\beta_I}{\beta_R} = \frac{k_{xI}}{k_{xR}} = \frac{k_{yI}}{k_{yR}} = \frac{1}{S} \tag{2.22}$$

At this stage, it is possible to integrate (2.13) only with respect to the real part of k_x and k_y provided a few modifications [6].

Starting from (2.13) and considering the following polar coordinates of k_x and k_y:

$$k_x = \beta\ cos(\alpha), \tag{2.23}$$

$$k_y = \beta\ sin(\alpha), \tag{2.24}$$

$$\beta = \sqrt{({k_x}^2 + {k_y}^2)}, \tag{2.25}$$

the integral resulting from the change of variable reads:

$$\begin{aligned} E_p(x,y,z) = \frac{-jk\eta}{(2\pi)^2} \int_\beta \int_\alpha F_p(k_x,k_y) \frac{exp\left(-j(\beta cos(\alpha)x + \beta sin(\alpha)y - k_z z)\right)}{2jk_z} \\ \left|det\left(J(\beta cos(\alpha), \beta sin(\alpha))\right)\right| \ d\alpha\ d\beta \end{aligned} \tag{2.26}$$

where $J(\beta cos(\alpha), \beta sin(\alpha))$ is the Jacobian of the transform. The determinant of the Jacobian produces: $|det\left(J(\beta cos(\alpha), \beta sin(\alpha))\right)| = \beta$.

The integral should now be computed with the real part of β and, as we know that $\beta = \beta_R + j\beta_I$, it can be written as follows:

$$\begin{aligned} E_p(x,y,z) = \frac{-jk\eta}{(2\pi)^2} \int_\beta \int_\alpha F_p(k_x,k_y) \frac{exp\left(-j(\beta cos(\alpha)x + \beta sin(\alpha)y - k_z z)\right)}{2jk_z} \\ \beta_R \left(1 + j\frac{\beta_I}{\beta_R}\right)\left(1 + j\frac{d\beta_I}{d\beta_R}\right)\ d\alpha\ d\beta_R \end{aligned} \tag{2.27}$$

Coming back to the real domain of k_x and k_y, the integral reads:

$$E_p(x,y,z) = \frac{-jk\eta}{(2\pi)^2} \int\int F_p(k_x,k_y) \frac{exp\left(-j(k_x x + k_y y - k_z z)\right)}{2jk_z} \left(1 + j\frac{\beta_I}{\beta_R}\right)\left(1 + j\frac{d\beta_I}{d\beta_R}\right)\ dk_{xR}\ dk_{yR}. \tag{2.28}$$

If we consider the SDP contour deformation, the following results can be inferred:

$$\frac{\beta_I}{\beta_R} = \frac{1}{S}, \tag{2.29}$$

$$\frac{d\beta_I}{d\beta_R} = \frac{1}{S^3}, \tag{2.30}$$

$$E_p(x,y,z) = \frac{-jk\eta}{(2\pi)^2} \int\int F_p(k_x,k_y) \frac{exp\left(-j(k_x x + k_y y - k_z z)\right)}{2jk_z} \left(1 + \frac{j}{S}\right)\left(1 + \frac{j}{S^3}\right)\ dk_{xR}\ dk_{yR}. \tag{2.31}$$

Thanks to this result, we can restrict ourselves to the integration with the real parts of (k_x, k_y).

2.4 Validation

In this section, we validate the approximation of the electric field using the method of decomposition into inhomogeneous plane waves as described in the previous section.

2.4.1 Validation using a z-oriented point source

We first consider a z-oriented unit point source for which the exact solution of the radiated field reads [9]:

$$\overrightarrow{E} = \frac{e^{-jkr}}{4\pi r}\left(\hat{a_\theta}\ sin(\theta)jk\eta\left(1-\frac{j}{kr}-\frac{1}{(kr)^2}\right)+\hat{a_r}\ cos(\theta)\frac{2\eta}{r}\left(1-\frac{j}{kr}\right)\right). \tag{2.32}$$

We are interested in the field radiated just below the source. Accordingly, we place the point source at a height $z=\frac{\lambda}{2}\ m$ and we compute the field on a $[\lambda \times \lambda]\ m^2$ square considering a 110 MHz frequency. Hence a frequency used in the LFAA bandwidth.

The Figures 2.2 and 2.3 represent the E_x, E_y, E_z components of the exact solution.

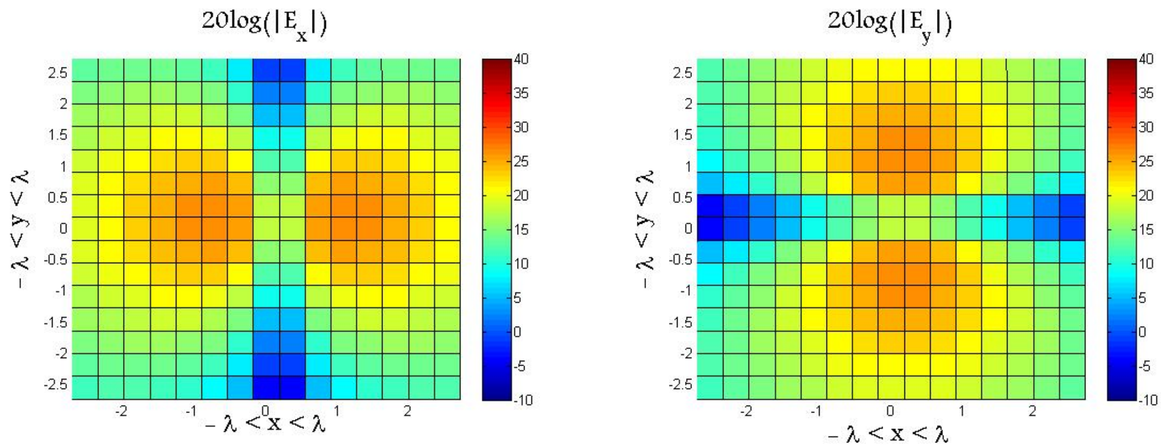

Figure 2.2: Exact x and y components of the electric field for a z-oriented point source

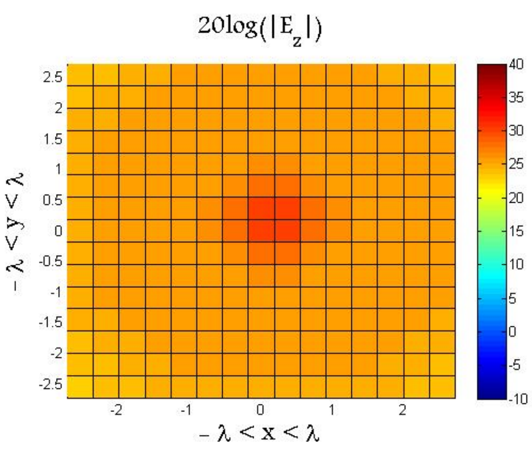

Figure 2.3: Exact z component of the electric field for a z-oriented point source

After that, the field can be estimated using the spectral approach. We obtain the results depicted in the Figures 2.4 and 2.5 using a $[64 \times 64]$ table of inhomogeneous plane waves with the SDP contour. The accuracy of the result depends on the number of plane waves considered. The required number of waves decreases with increasing distance between the observation point and the source.

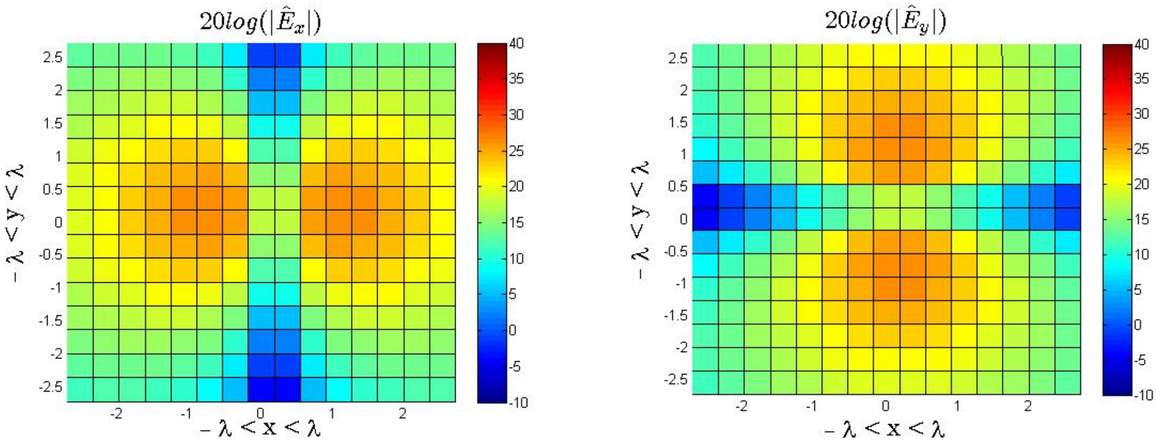

Figure 2.4: Approximated x and y components of the electric field for a z-oriented point source

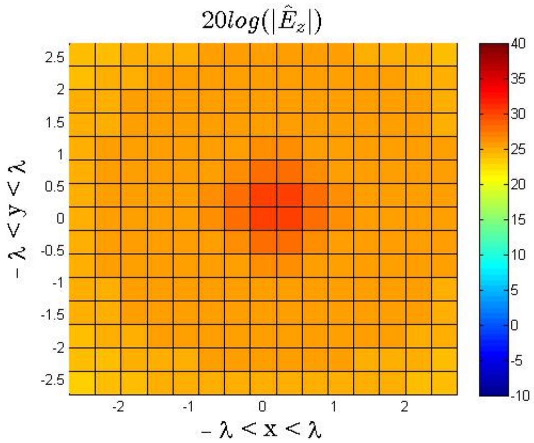

Figure 2.5: Approximated z component of the electric field for a z-oriented point source

The error along the axis $x = \lambda$ is given in Figures 2.6 , 2.7 and 2.8. The approximation is supposed good enough when the error is more than 30 dB under the superposition of the exact and the approximate solution.

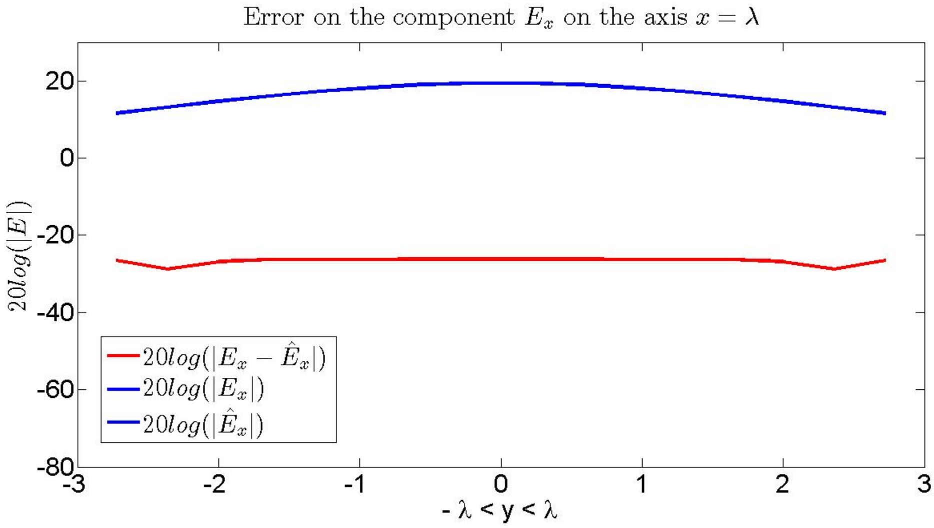

Figure 2.6:

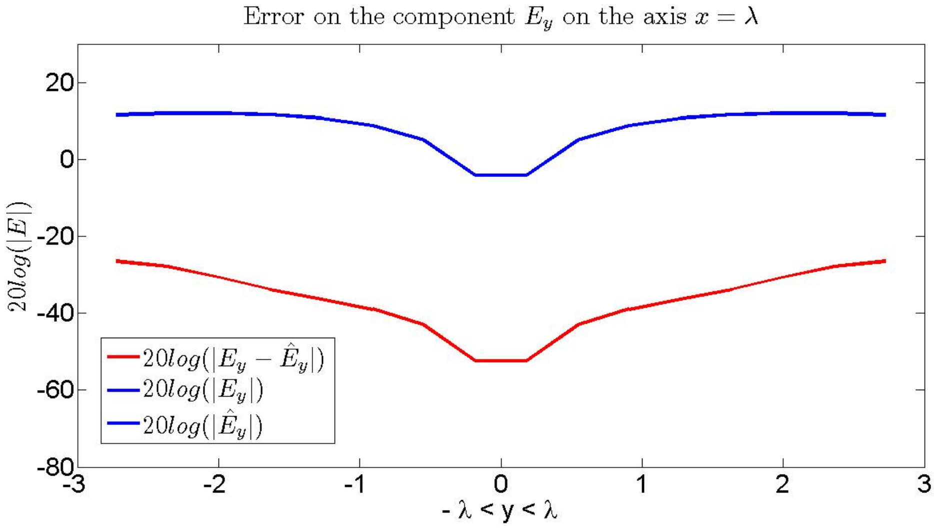

Figure 2.7:

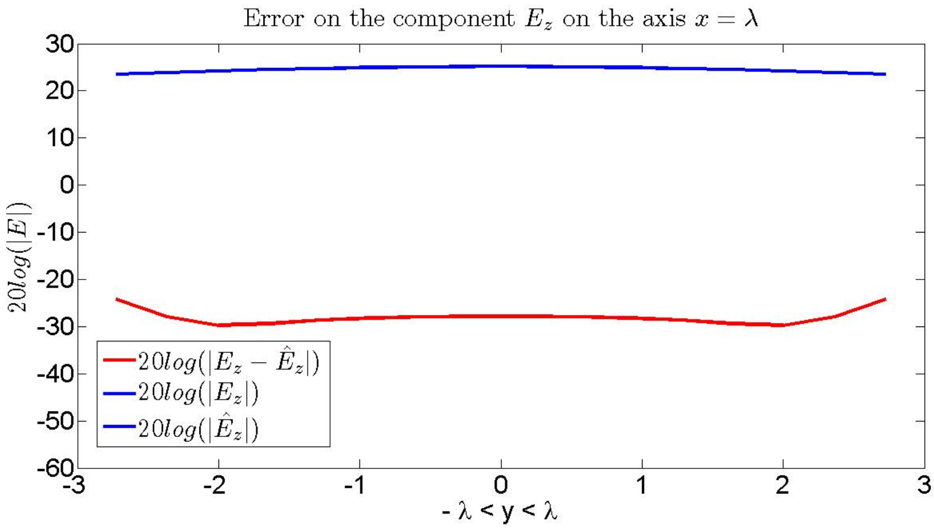

Figure 2.8:

2.4.2 Validation using a y-oriented point source

The same procedure can be applied to a y-oriented point source.

First of all, we need to find the exact expression of the radiated field.
The following development is similar to the one done for a z-oriented point source in [7].

Assuming an infinitesimal y-oriented dipole, the expression of the potential vector reads:

$$\overrightarrow{A} = \frac{\mu}{4\pi} \int \delta(x,y,z)\ \hat{a_y}\ \frac{e^{-jkr}}{r} dr' \tag{2.33}$$

We can derive the spherical coordinates of the potential vector in equation (2.33) using the rectangular to spherical transform given by the following matrix:

$$\begin{bmatrix} A_r \\ A_\theta \\ A_\phi \end{bmatrix} = \begin{bmatrix} sin(\theta)cos(\phi) & sin(\theta)sin(\phi) & cos(\theta) \\ cos(\theta)cos(\phi) & cos(\theta)sin(\phi) & -sin(\theta) \\ -sin(\phi) & cos(\phi) & 0 \end{bmatrix} \begin{bmatrix} A_x \\ A_y \\ A_z \end{bmatrix}. \tag{2.34}$$

Leading to the following spherical coordinates:

$$\begin{aligned} A_r &= sin(\theta)\ sin(\phi) \frac{\mu}{4\pi r} e^{-jkr}, \\ A_\theta &= cos(\theta)\ sin(\phi) \frac{\mu}{4\pi r} e^{-jkr}, \\ A_\phi &= cos(\phi) \frac{\mu}{4\pi r} e^{-jkr}. \end{aligned} \tag{2.35}$$

Given that $\overrightarrow{H} = \frac{1}{\mu}\left(\nabla \times \overrightarrow{A}\right)$, the magnetic field produces:

$$\begin{aligned} H_r &= 0, \\ H_\theta &= jk\ cos(\phi) \frac{e^{-jkr}}{4\pi r} \left(1 + \frac{1}{jkr}\right), \\ H_\phi &= jk\ cos(\theta)\ sin(\phi) \frac{e^{-jkr}}{4\pi r} \left(-1 - \frac{1}{jkr}\right). \end{aligned} \tag{2.36}$$

Knowing that $\overrightarrow{E} = \frac{1}{j\omega\epsilon}\left(\nabla \times \overrightarrow{H}\right)$, the electric field can be inferred:

$$\begin{aligned} E_r &= \eta\ sin(\theta)\ sin(\phi) \frac{e^{-jkr}}{2\pi r^2} \left(1 + \frac{1}{jkr}\right), \\ E_\theta &= jk\eta\ sin(\theta)\ cos(\phi) \frac{e^{-jkr}}{4\pi r} \left(-1 - \frac{1}{jkr} + \frac{1}{(kr)^2}\right), \\ E_\phi &= jk\eta\ cos(\phi) \frac{e^{-jkr}}{4\pi r} \left(-1 - \frac{1}{jkr} + \frac{1}{(kr)^2}\right). \end{aligned} \tag{2.37}$$

The electric field radiated by the y-oriented source at a height: $z = \frac{\lambda}{2}\ m$ is pictured in Figures 2.9 and 2.10.

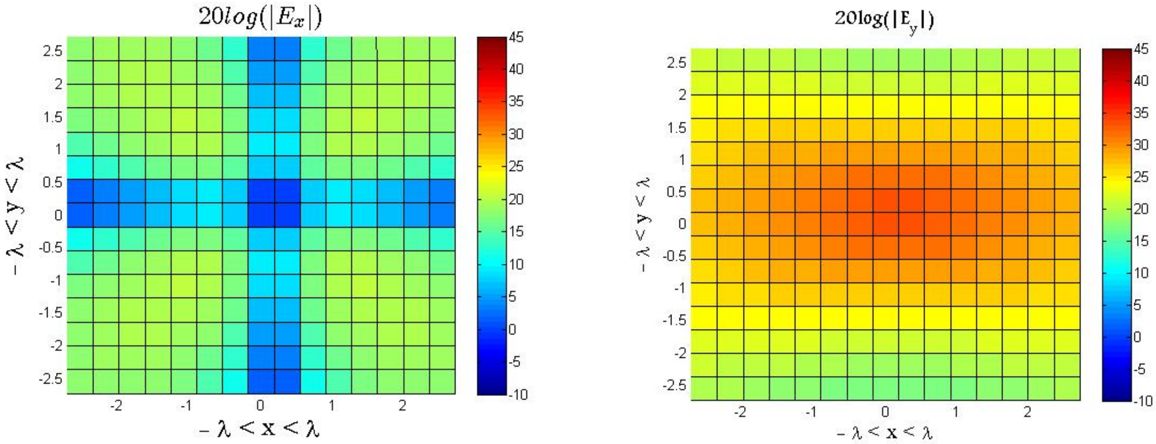

Figure 2.9: Exact x and y components of the electric field for a y-oriented point source

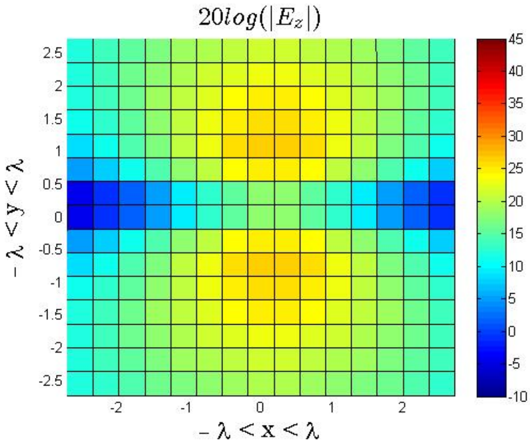

Figure 2.10: Exact z component for a y-oriented point source

Using the spectral approach with a $[64 \times 64]$ table of plane waves with the SDP contour, we obtain the results depicted in Figures 2.11 and 2.12.

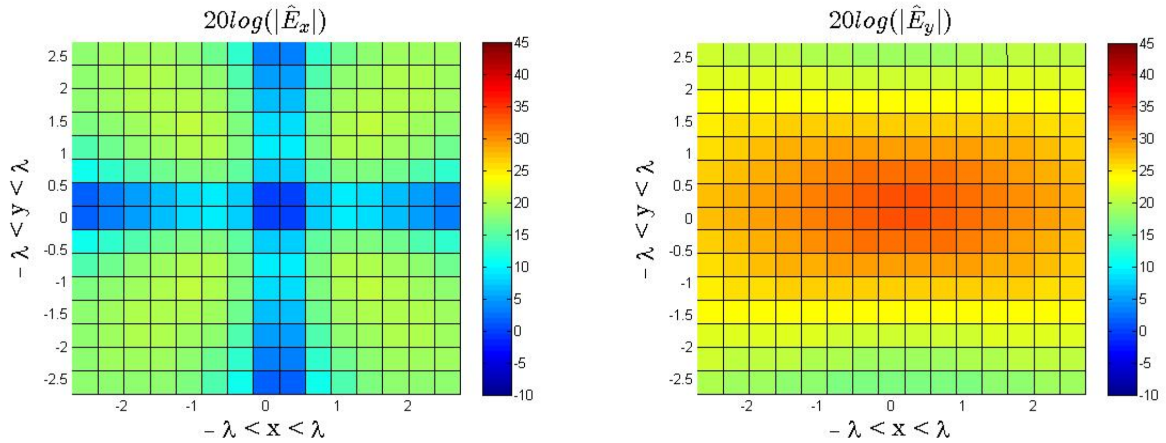

Figure 2.11: Approximated x and y components of the electric field for a y-oriented point source

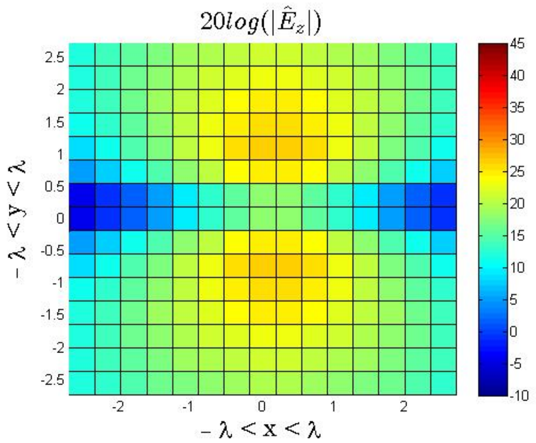

Figure 2.12: Approximated z component of the electric field for a y-oriented point source

The error on the axis $x = \lambda$ is pictured in Figures 2.13, 2.14 and 2.15. The error is again less than 30 dB under the superposition of the solution and the approximation.

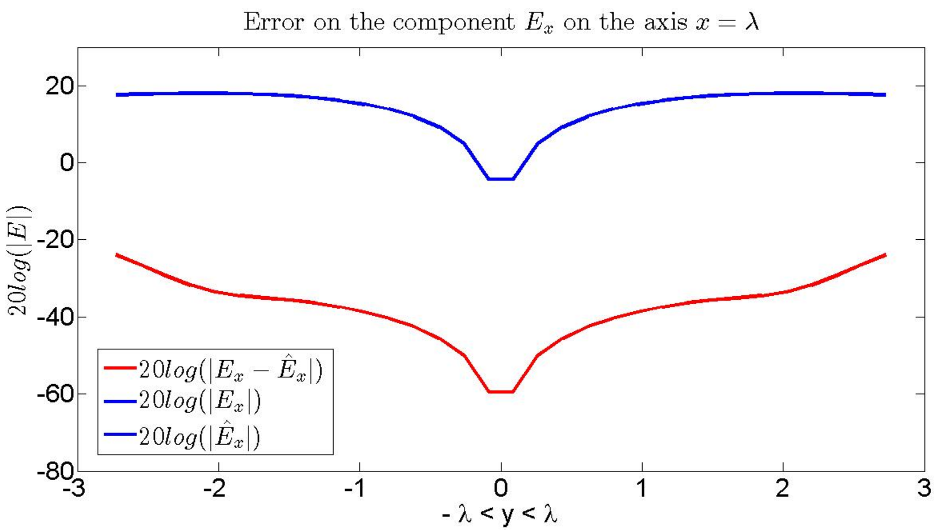

Figure 2.13:

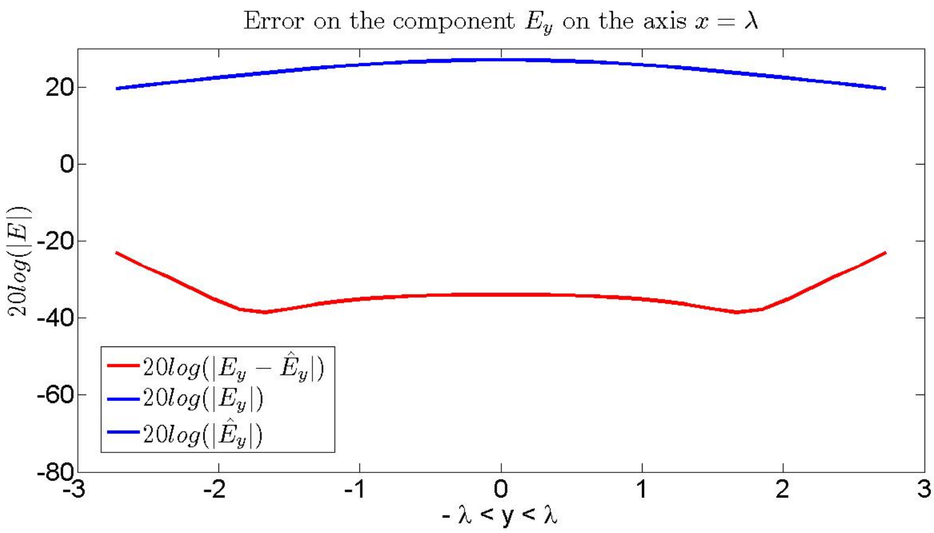

Figure 2.14:

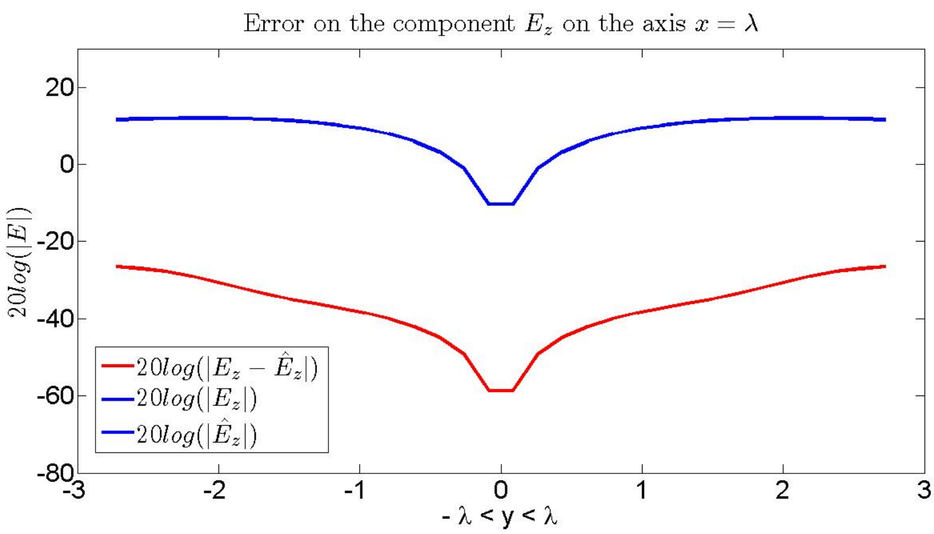

Figure 2.15:

The precision of the method is improved when a larger number of plane waves is considered. The Figure 2.16 shows the error for diverse values of nk, considering a $[nk \times nk]$ table of plane waves and a SDP contour deformation for a z-oriented point source.

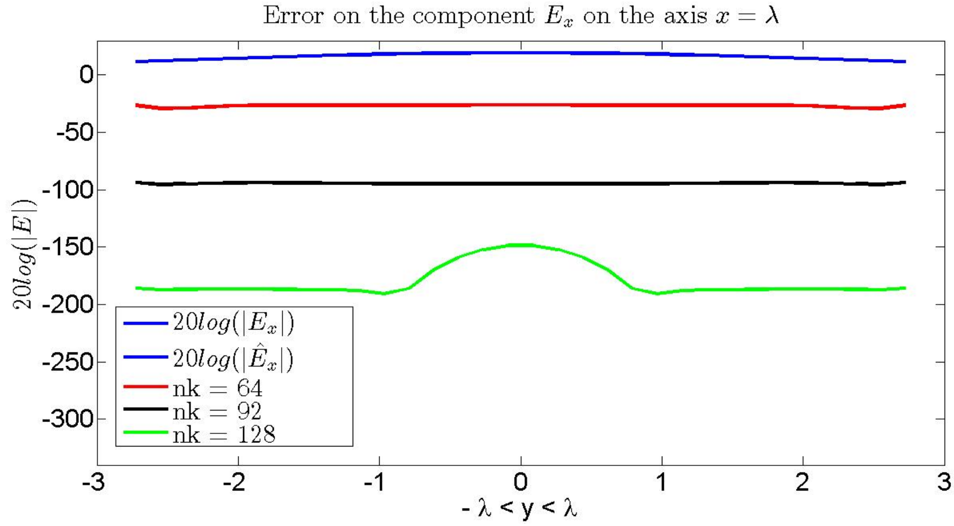

Figure 2.16:

The same error is plotted with a y-oriented point source in Figure 2.17.

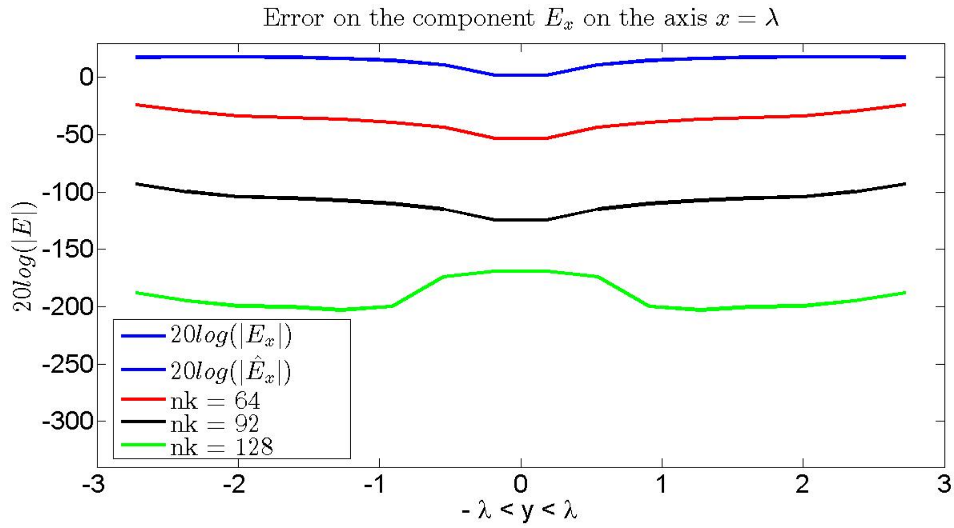

Figure 2.17:

2.5 Compensation between aliasing and truncation error

The method of decomposition into inhomogeneous plane waves owns a remarkable property when considering the SDP contour deformation. If we consider a domain of integration $[-k_{max}, k_{max}]$ discretized into nk points, the combination of well selected k_{max} and nk can lead to a compensation between aliasing and truncation errors in equation (2.31) [4] [8].

This compensation is due to the resemblance between the integral in equation (2.31) and the Fourier transform of a Gaussian function with standard deviation close to $(k/2z)^{\frac{1}{2}}$, with k the wavenumber and z the distance between the source and the antenna. A relation can then be established between the normalized half width of the integration domain $\frac{k_{max}}{\sigma}$ and the number of points nk.

Due to this property, the numerical integration leading to the estimation of the field in (2.31) converges rapidly with a simple integration using rectangles. When using higher order numerical integration methods, the compensation of errors is less pronounced and the convergence is slower.

One can see the different errors made when estimating the E_x component of the radiated field of a z-oriented point source with, on the one hand, a simpson numerical integration method and, on the other hand, an integration with rectangles in Figure 2.18. The integration is computed here with a table of $[64 \times 64]$ plane waves.

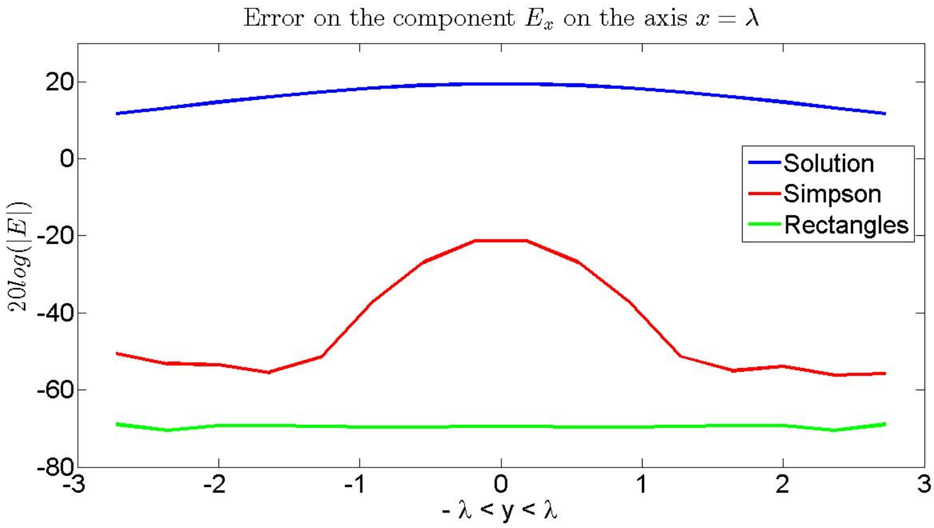

Figure 2.18: Error on the estimated field considering integration with simpson and rectangles methods

This result can also be compared to the previous results obtained for the z-oriented point source in Figure 2.6. Another choice of domain range has been made here to show that, even with the same number of plane waves, the error can be significantly lowered (or increased) when taking another k_{max}. As an example, the k_{max} considered here is equal to 7 k and the k_{max} leading to the result in Figure 2.6 is equal to 9 k, with k the wavenumber.

2.6 Choice of the contour deformation

We have seen so far that the SDP contour deformation can give good results. Unfortunately, the quality of the approximation decreases with decreasing distance between the source and the observation point. However, it appears that considering a lower contour deformation gives better results in these circumstances. Let us consider a new contour deformation given by:

$$S_2 = 1 \, / \, (A \; exp(-\beta_R/k)) \tag{2.38}$$

with A a carefully chosen constant. The relation between the imaginary and the real parts of β produces now $\beta_I = \beta_R \, / S_2$.

Let us call this contour: " the exponential contour". The SDP contour and the exponential contour are depicted in Figure 2.19. One can see that the exponential contour (plotted here with A = 0.7) is significantly lower than the SDP contour.

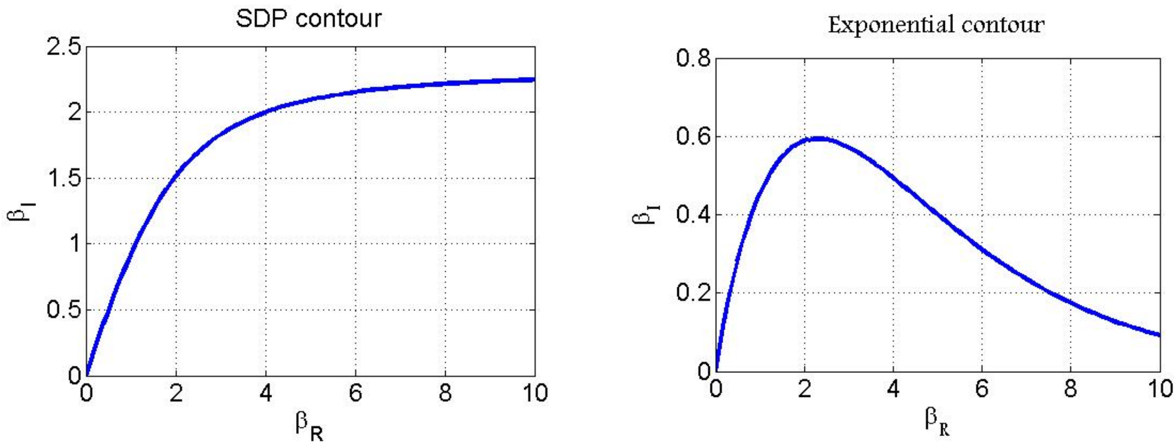

Figure 2.19: Comparison between the SDP and the exponential contours

Let us consider a z-oriented point source at a $z = \frac{\lambda}{6}\ m$ height. The x component of the radiated field is estimated in Figure 2.20 with the two different contours of Figure 2.19 considering a $[64 \times 64]$ table of plane waves.

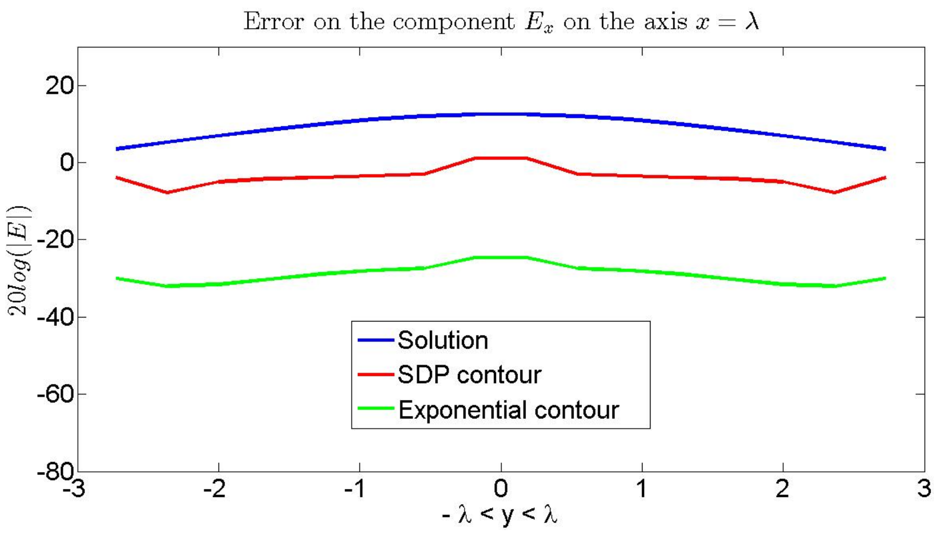

Figure 2.20: Comparison between the approximations considering the SDP and the exponential contour deformations

The exponential contour gives better performance and the result obtained with the SDP contour is not acceptable anymore. The SDP contour would need more plane waves to achieve a good result and thus would take a longer execution time.

The exponential contour needs to be considered due to the geometry of the SKALA antenna. Indeed, some of the arms of the antenna are very close to the ground plane. The lowest arm of the antenna is placed at a 0.18 m height (which is close to $\frac{\lambda}{15}$ at a 110 MHz frequency).

2.7 Determination of the reflection coefficients at a single interface

In this section, a formulation of the reflection coefficients [10] for both TE and TM waves is given. The need for the reflected field will appear when computing the projection of the total field (incident and reflected) on the testing functions in order to compute the current induced in the ground plane as will be seen in Chapter 3.

Considering two semi-infinite media as depicted in Figure 2.1, a plane wave reaching the boundary induces a reflected wave and a transmitted wave.

The reflection coefficient is defined here as the ratio of the incident wave to the reflected wave:

$$\begin{aligned}\Gamma^u &= \frac{E^{u-}}{E^{u+}}\\ \Gamma^d &= \frac{E^{d+}}{E^{d-}}\end{aligned} \tag{2.39}$$

where u and d respectively denote the upper and lower media.

As the TE and TM waves are orthogonal to each other, they give the advantage of dealing with the Γ coefficients independently. As a result, the Γ_{TE} and Γ_{TM} reflection coefficients can be calculated separately and they only need to be recombined in the final solution.

Given an interface with no sources, the reflection coefficients can be determined by enforcing the following boundary conditions:

$$\begin{aligned}\hat{z} \times E^u &= \hat{z} \times E^d\\ \hat{z} \times H^u &= \hat{z} \times H^d.\end{aligned} \tag{2.40}$$

These equations mean that the electric and magnetic fields need to be continuous across the interface.

Let us consider the following relations:

$$\hat{z} \times \hat{e}^u = \frac{ct_u}{\beta} \begin{bmatrix} -k_y \\ k_x \\ 0 \end{bmatrix} = \pm \frac{ct_u}{ct_d}\ \hat{z} \times \hat{e}^{\pm}, \tag{2.41}$$

$$ct \triangleq \frac{k_z}{k} = cos(\theta) \tag{2.42}$$

where θ is the elevation angle of $\hat{k}$ in the layer considered.

Placing the interface on the plane $z = 0$ and imposing the equations (2.40), the reflection coefficients at a single interface read:

$$\begin{aligned} \Gamma_{TE}^{u} &= \frac{ct_u\eta_d + ct_d\eta_u}{ct_u\eta_d - ct_d\eta_u} \\ \Gamma_{TM}^{u} &= \frac{ct_u\eta_u + ct_d\eta_d}{ct_u\eta_u - ct_d\eta_d} \end{aligned} \tag{2.43}$$

for the upper medium and

$$\begin{aligned} \Gamma_{TE}^{d} &= \frac{ct_d\eta_u + ct_u\eta_d}{ct_d\eta_u - ct_u\eta_d} \\ \Gamma_{TM}^{d} &= \frac{ct_d\eta_d + ct_u\eta_u}{ct_d\eta_d - ct_u\eta_u} \end{aligned} \tag{2.44}$$

for the lower medium.

The calculations leading to (2.43) are described in Annex A.

2.8 Conclusion

Thanks to the spectral approach described in this chapter, we can now estimate the radiated field of any given source on a finite ground plane. The next step consists in computing the current induced in the ground plane from the incident field and will be investigated in the following chapter.

Chapter 3

Method of Moments

This chapter gives an introduction on the basis of the Method of Moments and explains how the current induced in the finite ground plane will be computed.

Basically, once the electric field is calculated on the finite ground plane, the Method of Moments permits us to find the induced current in the ground plane by resolving a linear system of equations.

3.1 Definition

The Method of Moments [11], [12], [14] is a numerical tool used to solve electromagnetic systems with integral equations representing radiation and scattering problems. The general form of the system to solve is the following:

$$\mathcal{L}f = g \tag{3.1}$$

where $\mathcal{L}$ is a linear integro-differential operator, g is a known excitation and f is the function to be determined.

The unknown function f can represent quantities such as charge or current and can be expanded in a set of functions f_n as follows:

$$f = \sum_n \alpha_n f_n \tag{3.2}$$

where α_n are constants and f_n are the so-called basis functions.

The basis functions are used here to model the behavior of the unknown function f.

After that, a set of N testing functions w_m can be chosen and an inner product $< .,. >$ can be defined. Applying the inner product to (3.1) with one of the testing functions produces:

$$\sum \alpha_n < \mathcal{L}f_n, w_m >=< g, w_m > . \tag{3.3}$$

As a result, the problem can be expressed as a $N \times N$ system of equations as follows:

$$[Z_{mn}][\alpha_n] = [g_m] \tag{3.4}$$

with $Z_{mn} =< \mathcal{L}f_n, w_m >$ and $g_m =< g, w_m >$.

3.2 Basis functions

The domain of the unknown function f will be discretized into non-overlapping sub-domains using the software Gmsh [13] and equivalent currents will be estimated on each of them. According to the geometry, a type of basis function can be chosen. In this work, the types of basis function used are rooftop and Rao-Wilton-Glisson (RWG) basis functions.

3.2.1 Rooftop basis function

Let us consider a simple rectangular domain on which we discretize the x, y coordinates into a set of points $(x_i, y_i), i = 0, 1, .., M$.

The rooftop basis function is the combination of two basic functions: a triangular function in one direction and a rectangular function in the direction orthogonal to the first one.

Basically, it can be expressed as:

$$\overrightarrow{J_x}(x,y) = \left(1 - \frac{|x|}{d_x}\right) rect\left(\frac{y}{W_y}\right)\hat{x} \tag{3.5}$$

for a x-oriented basis function with $|x| \leq d_x$ and $d_x = x_{i+1} - x_i$.

Accordingly, the y-oriented basis function is expressed as:

$$\overrightarrow{J_y}(x,y) = \left(1 - \frac{|y|}{d_y}\right) rect\left(\frac{x}{W_x}\right)\hat{y} \tag{3.6}$$

with $|y| \leq d_y$ and $d_y = y_{i+1} - y_i$.

The x and y-oriented rooftop basis functions are pictured in Figure 3.1.

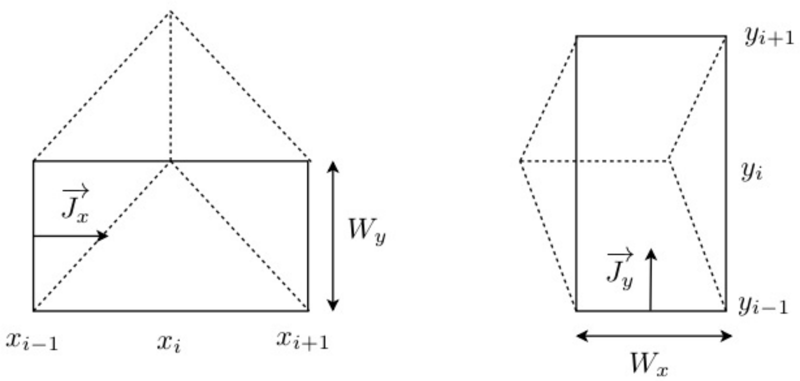

Figure 3.1: x and y-oriented rooftop basis functions

This type of basis function will be used to describe the current on a patch antenna in the validation part.

3.2.2 RWG basis function

When the geometry to discretize is more complicated, the RWG basis function can be considered on a triangular mesh.

Considering the domain pictured in Figure 3.2, the basis function can be described as follows:

$$\vec{J}(x,y) = \frac{\vec{r}(x,y) - \vec{r_0}}{h_n^+} \tag{3.7}$$

if $(x,y) \in S_n^+$ and

$$\vec{J}(x,y) = \frac{\vec{r_1} - \vec{r}(x,y)}{h_n^-} \tag{3.8}$$

if $(x,y) \in S_n^-$.

h_n^+ and h_n^- respectively represent the height of the triangles described by S_n^+ and S_n^- and $\vec{r_0}$, $\vec{r_1}$ are the coordinates of the external edges of the triangles.

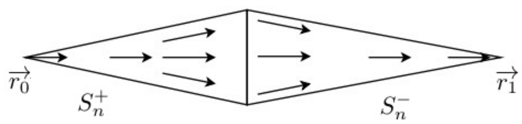

Figure 3.2: RWG basis functions

In this work, the finite ground plane will be described with a triangular mesh. Thus, the RWG basis function will be considered.

3.3 Application of the Method of Moments

The Method of Moments will be used to find the current induced on the finite ground plane considering the incident field radiated by an arbitrary source.

The steps to find the current are the following:

1. Compute the incident and reflected fields.
2. Discretize the ground plane.
3. Integrate the projection of the field on the testing functions.
4. Solve the MoM linear system of equations.

The incident field is computed using the decomposition into inhomogeneous plane waves described in Chapter 2. The mesh describing the finite ground plane is pictured in Figure 3.3.

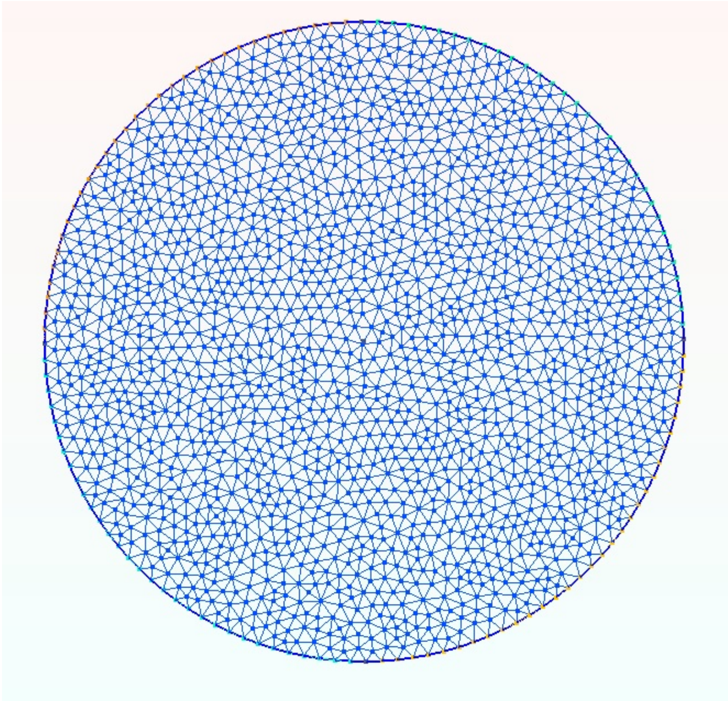

Figure 3.3: Mesh describing the finite ground plane obtained with the Gmsh software

Let us define $\overrightarrow{J}$ the current on the ground plane which can be decomposed into a series of N basis functions:

$$\overrightarrow{J} = \sum_{j=0}^{N} \alpha_j \ \overrightarrow{J}_j \tag{3.9}$$

Considering $\overrightarrow{E^i}$ as the summation of the incident field and the reflected field, and $\overrightarrow{E^s}\left(\overrightarrow{J}\right)$ the field scattered by the whole current distribution, a relation involving the two fields can be found at the boundary between the two media:

$$\overrightarrow{E^i} + \overrightarrow{E^s}\left(\overrightarrow{J}\right) = 0. \tag{3.10}$$

The inner product of the Method of Moments described above can be chosen as the integral of the projection of the fields on the testing functions $\overrightarrow{J_{t_i}}$. Applying this inner product to (3.10) produces:

$$\int \overrightarrow{E^s}\left(\overrightarrow{J}\right) \cdot \overrightarrow{J_{t_i}} \ dS = -\int \overrightarrow{E^i} \cdot \overrightarrow{J_{t_i}} \ dS \tag{3.11}$$

where S represents the finite ground plane.

In this case, the chosen testing functions correspond to the basis functions of the ground plane.

Using the series representation of the current $\overrightarrow{J}$, (3.11) can also be expressed as:

$$\sum_{j=0}^{N} \alpha_j \int \overrightarrow{E^s}\left(\overrightarrow{J_j}\right) \cdot \overrightarrow{J_{t_i}} \ dS = -\int \overrightarrow{E^i} \cdot \overrightarrow{J_{t_i}} \ dS \tag{3.12}$$

which can be written in matrix form as follows:

$$[Z_{ij}][\alpha_j] = -[v_i] \tag{3.13}$$

The calculation of the Method of Moments matrix Z in equation (3.13) will be performed using a routine developed at UCL. The approach in this routine is based on the layered medium Green functions [11], [10]. As we consider that the Z matrix is known in this work, the main point is the calculation of the so-called excitation vector present in the right side of equation (3.13). Once this vector is calculated, one only needs to multiply it by the inverse of the Z matrix to find the induced current.

Furthermore, the radiation pattern of the ground carrying the induced current will be calculated using a routine from UCL based as well on the layered medium Green functions.

3.4 Conclusion

In this chapter, a method to compute the current induced in the ground plane has been described. Nevertheless, this method is based on the integration of a continuous field. We will see in the next chapter how to solve the integral only with a few points per testing function.

Chapter 4

Quadratures

A method to compute the field incident to the finite ground plane has been described in Chapter 2. The incident field should be projected on some testing functions in order to calculate the excitation vector as explained in Chapter 3. Unfortunately, the field incident to the ground plane is only known on a finite number of points. However, the integral of the projection of the field on a triangular testing function can be performed with a few points using quadratures.

In this chapter, some Gaussian quadratures for triangles are described then an approximation of the integral of the right side of equation (3.12) is given.

4.1 Gaussian quadratures for triangles

The general problem consists in approximating the integral I of a given function G on an arbitrary triangular element S. This integral can be written as:

$$I = \int \int_S G(x, y)\ dx\ dy. \tag{4.1}$$

In our case, the G function represents the projection of the incident field on the testing function and is only known on a finite number of points. Using quadratures, the integral in (4.1) can be estimated using some chosen points with corresponding weights:

$$I \simeq \frac{1}{2} \sum_i\ w_i G(x_i, y_i). \tag{4.2}$$

The weights are given by the Gaussian quadrature for triangular elements. A set of them are depicted in Figure 4.1.

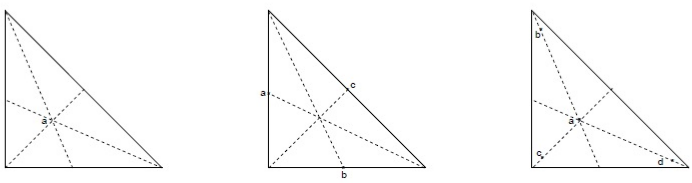

(a) Linear
$a = \left(\frac{1}{3}, \frac{1}{3}\right),\ w = 1$

(b) Quadratic
$a = \left(0, \frac{1}{2}\right),\ w = \frac{1}{3}$
$b = \left(\frac{1}{2}, 0\right),\ w = \frac{1}{3}$
$c = \left(\frac{1}{2}, \frac{1}{2}\right),\ w = \frac{1}{3}$

(c) Cubic
$a = \left(\frac{1}{3}, \frac{1}{3}\right),\ w = -\frac{27}{48}$
$b = \left(\frac{2}{15}, \frac{11}{15}\right),\ w = \frac{25}{48}$
$c = \left(\frac{2}{15}, \frac{2}{15}\right),\ w = \frac{25}{48}$
$d = \left(\frac{11}{15}, \frac{2}{15}\right),\ w = \frac{25}{48}$

Figure 4.1: Quadrature for triangular elements [15]

Even though the Gaussian quadrature is defined on this type of triangle, the integral I of equation (4.1) needs to be estimated on any arbitrary triangle. A mapping between a given triangle and the one presented in Figure 4.1 needs to be performed. This mapping can be done using nodal shape [15],[16].

Let us define the nodal shape functions $Q(\alpha, \beta)$ and $T(\alpha, \beta)$ as the mapping between the (x, y) coordinates of the arbitrary triangle and the (α, β) coordinates of the regular triangle. This mapping is illustrated in Figure 4.2.

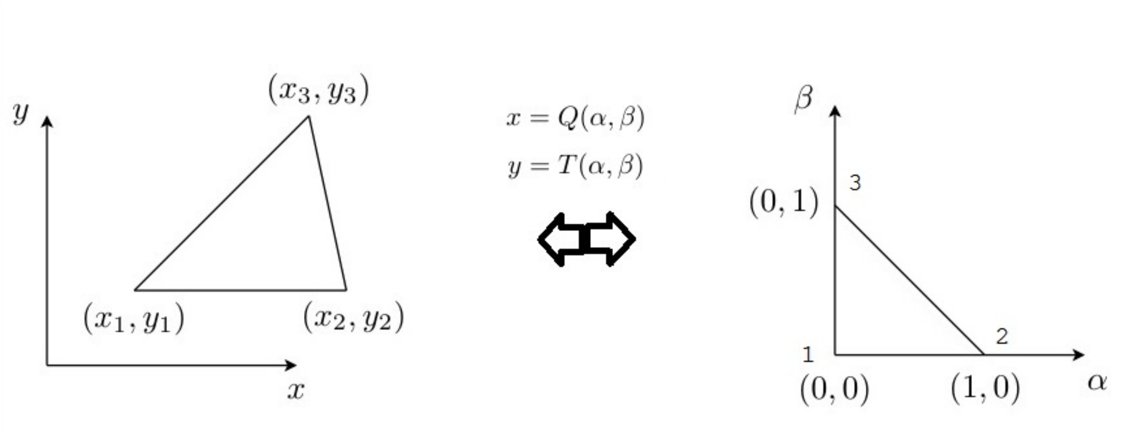

Figure 4.2: Mapping between the two triangles

The nodal shape functions M_1, M_2, M_3 for triangles are the followings:

$$\begin{aligned} M_1(\alpha, \beta) &= 1 - \alpha - \beta, \\ M_2(\alpha, \beta) &= \alpha, \\ M_3(\alpha, \beta) &= \beta. \end{aligned} \tag{4.3}$$

The mapping using nodal shape functions can be achieved as follows:

$$\begin{aligned} x = Q(\alpha, \beta) = x_1 M_1(\alpha, \beta) + x_2 M_2(\alpha, \beta) + x_3 M_3(\alpha, \beta), \\ y = T(\alpha, \beta) = y_1 M_1(\alpha, \beta) + y_2 M_2(\alpha, \beta) + y_3 M_3(\alpha, \beta), \end{aligned} \tag{4.4}$$

where the coordinates (x_1, y_1), (x_2, y_2) and (x_3, y_3) correspond to the coordinates of the edges of the arbitrary triangle.

After that, the integral on the arbitrary triangle needs to be mapped into an integral on the regular triangle. Considering (4.1), a change of variable produces:

$$I = \int \int_{S'} G(x, y) dx dy = \int \int_{S} G(Q(\alpha, \beta), T(\alpha, \beta)) |J(\alpha, \beta)| \; d\alpha \; d\beta \tag{4.5}$$

where S' characterizes the arbitrary triangle and $J(\alpha, \beta)$ represents the Jacobian of the transformation.

Denoting $A_{S'}$ as the area of the arbitrary triangle S', the Jacobian reads:

$$|J(\alpha, \beta)| = 2 * A_{S'} \tag{4.6}$$

where

$$A_{S'} = \frac{|x_1(y_2 - y_3) + x_2(y_3 - y_1) + x_3(y_1 - y_2)|}{2}. \tag{4.7}$$

From there, the integral I can be expressed as:

$$I = 2A_{S'} \int \int_{S'} G(Q(\alpha, \beta), T(\alpha, \beta))\ d\alpha\ d\beta. \tag{4.8}$$

Replacing the integral by a sum with one of the N points Gaussian quadrature shown in Figure 4.1 yields:

$$I = A_{S'} \sum_{i=0}^{N} w_i G(Q(\alpha_i, \beta_i), T(\alpha_i, \beta_i)). \tag{4.9}$$

It is also important to know that a Gaussian quadrature of N points performs perfectly the integration of a N-1 degree polynomial.

4.2 Integration of the electric field over a testing function

The following integral corresponding to the right side of equation (3.12) can now be approximated using a few values of the incident field:

$$-\int \overrightarrow{E^i} \cdot \overrightarrow{J_{t_i}}\ dS. \tag{4.10}$$

Let us consider the triangular testing function depicted in Figure 4.3 and denote h_n^+ and h_n^- the heights of the triangles S_n^+ and S_n^-. In this example, a $N = 3$ points Gaussian quadrature is considered.

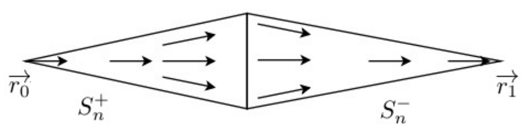

Figure 4.3: RWG basis functions

The integral in equation (4.10) can be decomposed into two sub-integrals: one for the rising side in S_n^+ of the testing function and one for the decaying side in S_n^- of the testing function.

Considering first the rising side, the value of the testing function produces:

$$\frac{\overrightarrow{r_i} - \overrightarrow{r_0}}{h_n^+} \tag{4.11}$$

for a given point described by the coordinate vector $\overrightarrow{r_i}$.

Choosing the three points corresponding to the centers of the three edges, the integral for the rising side can be approximated as follows:

$$-\frac{A_n^+}{h_n^+}\sum_{i=0}^{3} w_i[\overrightarrow{E}(\overrightarrow{r_i}) \cdot (\overrightarrow{r_i} - \overrightarrow{r_0})] \tag{4.12}$$

with A_n^+ the area of the triangle carrying the rising testing function.

Considering now the decaying side, the value of the testing function reads:

$$\frac{\overrightarrow{r_1} - \overrightarrow{r_i}}{h_n^+} \tag{4.13}$$

for a given point described by the coordinate vector $\overrightarrow{r_i}$.

The integral on the decaying side can be approximated by:

$$-\frac{A_n^-}{h_n^-}\sum_{i=0}^{3} w_i[\overrightarrow{E}(\overrightarrow{r_i}) \cdot (\overrightarrow{r_1} - \overrightarrow{r_i})] \tag{4.14}$$

with A_n^- the area of the triangle carrying the decaying testing function.

Finally, the approximation of equation (4.10) using a three points quadrature reads:

$$-\frac{A_n^+}{h_n^+}\sum_{i=0}^{3} w_i[\overrightarrow{E}(\overrightarrow{r_i}) \cdot (\overrightarrow{r_i} - \overrightarrow{r_0})] - \frac{A_n^-}{h_n^-}\sum_{i=0}^{3} w_i[\overrightarrow{E}(\overrightarrow{r_i}) \cdot (\overrightarrow{r_1} - \overrightarrow{r_i})]. \tag{4.15}$$

In the case of a three points quadrature, the weights w_i are all equal to $\frac{1}{3}$.

4.3 Conclusion

At this stage, we have all the background necessary to calculate the current induced in the ground plane by a given source. The next chapter is dedicated to the validation of this approach.

Chapter 5

Validation of the Method

In this chapter, the current induced in the finite ground plane is calculated for different sources using the methods described in Chapters 2, 3 and 4. A x-oriented basis function will be first considered then the method will be validated with a patch antenna.

The radiation pattern of the ground carrying this current will be compared to the one generated with a method developed at UCL which has been validated by the simulation software IE3D.

5.1 Validation with a x-oriented basis function

Let us consider a x-oriented basis function situated above the ground plane as depicted in Figure 5.1. The basis function is placed 0.5 m above the ground and a diameter of 6 m is considered for the finite ground plane. The coordinates of the basis function are described by three points: the edges $\overrightarrow{r_0}$ and $\overrightarrow{r_2}$ and the middle points $\overrightarrow{r_1}$. The chosen coordinates are the followings:

$$\begin{aligned} \overrightarrow{r_0} &= (-0.1, 0, 0.5) \\ \overrightarrow{r_1} &= (0, 0, 0.5) \\ \overrightarrow{r_2} &= (0.1, 0, 0.5) \end{aligned} \tag{5.1}$$

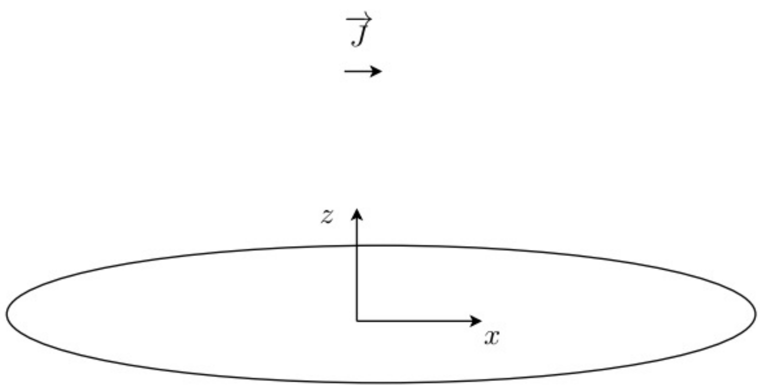

Figure 5.1: x-oriented basis function above the finite ground plane

The electric field radiated by the basis function is calculated using the method of decomposition into inhomogeneous plane waves described in Chapter 2.

Firstly, the radiation pattern of the basis function needs to be computed:

$$F_p(k_x, k_y) = \int\int\int_V \overrightarrow{J}(\overrightarrow{r}') \; exp\left(-j(k_x x' + k_y y' + k_z z')\right) dV \tag{5.2}$$

Here the integration is produced along a straight line.

The triangular basis function can be expressed as

$$\overrightarrow{J}(x, y) = s \; \frac{\overrightarrow{r_1} - \overrightarrow{r_0}}{||\overrightarrow{r_1} - \overrightarrow{r_0}||} \tag{5.3}$$

for the rising edge and,

$$\overrightarrow{J}(x, y) = (1 - s)\frac{\overrightarrow{r_2} - \overrightarrow{r_1}}{||\overrightarrow{r_2} - \overrightarrow{r_1}||} \tag{5.4}$$

for the decaying edge, with s going from 0 to 1 in both cases.

The point corresponding to the amplitude s is given by $\overrightarrow{r'} = \overrightarrow{r_0} + s(\overrightarrow{r1} - \overrightarrow{r_0})$ for the rising edge and $\overrightarrow{r'} = \overrightarrow{r_1} + s(\overrightarrow{r_2} - \overrightarrow{r_1})$ for the decaying edge.

The integration can now be performed by adding the integrals of both the rising edge and the decaying edge:

$$\begin{aligned} F_p(k_x, k_y) = &\int_0^1 s \; [\frac{\overrightarrow{r_1} - \overrightarrow{r_0}}{||\overrightarrow{r_1} - \overrightarrow{r_0}||} \cdot \hat{e_p}] \; exp\left(j(\overrightarrow{k} \cdot (\overrightarrow{r_0} + s(\overrightarrow{r1} - \overrightarrow{r_0})))\right) ds \\ &+ \int_0^1 (1 - s) \; [\frac{\overrightarrow{r_2} - \overrightarrow{r_1}}{||\overrightarrow{r_2} - \overrightarrow{r_1}||} \cdot \hat{e_p}] \; exp\left(j(\overrightarrow{k} \cdot (\overrightarrow{r_1} + s(\overrightarrow{r2} - \overrightarrow{r_1})))\right) ds \end{aligned} \tag{5.5}$$

where the product $\overrightarrow{k} \cdot \overrightarrow{r'}$ is defined as $k_x r'_x + k_y r'_y - k_z r'_z$ with $\overrightarrow{r'} = (r'_x, r'_y, r'_z)$ and where p represents the polarization (either TE or TM).

When introducing the following notations:

$$\begin{aligned} a_1 &= \overrightarrow{k} \cdot (\overrightarrow{r_1} - \overrightarrow{r_0}), \\ a_2 &= \overrightarrow{k} \cdot (\overrightarrow{r_2} - \overrightarrow{r_1}), \end{aligned} \tag{5.6}$$

the integral in equation (5.5) can be solved by parts and the result produces:

$$\begin{aligned} F_p(k_x, k_y) = &\, exp\left(j(\overrightarrow{k} \cdot \overrightarrow{r_0}\right) \; [\frac{\overrightarrow{r_1} - \overrightarrow{r_0}}{||\overrightarrow{r_1} - \overrightarrow{r_0}||} \cdot \hat{e_p}] \left(\frac{e^{(ja_1)}}{a_1} + \frac{e^{(ja_1)} - 1}{a_1^2}\right) \\ &+ exp\left(j(\overrightarrow{k} \cdot \overrightarrow{r_1}\right) \; [\frac{\overrightarrow{r_2} - \overrightarrow{r_1}}{||\overrightarrow{r_2} - \overrightarrow{r_1}||} \cdot \hat{e_p}] \left(\frac{-1}{ja_2} + \frac{-e^{(ja_2)} + 1}{a_2^2}\right) \end{aligned} \tag{5.7}$$

for a polarization $\hat{e_p}$.

The radiation pattern can then be calculated for both TE and TM polarizations and the field on the ground plane can be computed as follows:

$$E_p(x, y, z) = \frac{-jk\eta}{(2\pi)^2} \int\int F_p(k_x, k_y) \frac{exp\left(-j(k_x x + k_y y - k_z z)\right)}{2jk_z} \; dk_x \; dk_y. \tag{5.8}$$

After that, the field reflected by the ground plane has to be taken in account. The total tested field E_{tp} for polarization p is the result of the addition of the incident field and the reflected field:

$$E_{tp}(x, y, z) = E_p(x, y, z) + \frac{E_p(x, y, z)}{\Gamma_p} \tag{5.9}$$

with Γ_p the reflection coefficient for polarization p calculated with the equations (2.43).

Once the tested field is computed, the excitation vector on the ground plane can be obtained by computing the integration of the projection of the tested field on the testing functions as described in Chapter 3 . After that, the system of equations in (3.13) can be solved to find the induced current. As a reminder, the Method of Moment matrix Z as well as the radiation pattern of the ground plane are calculated using routines from UCL as explained in the end of Chapter 3.

The radiation pattern of the finite ground plane carrying the induced current is compared to the exact solution in Figure 5.2. The data called "IPW" (Inhomogeneous Plane Waves) is the one obtained with the method described here and the data called "traditional MoM" is the one from the method developed in UCL and validated with IE3D. The radiation pattern is shown here for azimuth angles $\phi = 0°$ and $\phi = 90°$. The plane characterized by $\phi = 0°$ is aligned with the x axis. One can see that the results overlap quite well.

The excitation vector has been calculated here at a 110 MHz frequency using a $[128 \times 128]$ table of plane waves and a 3 points quadrature.

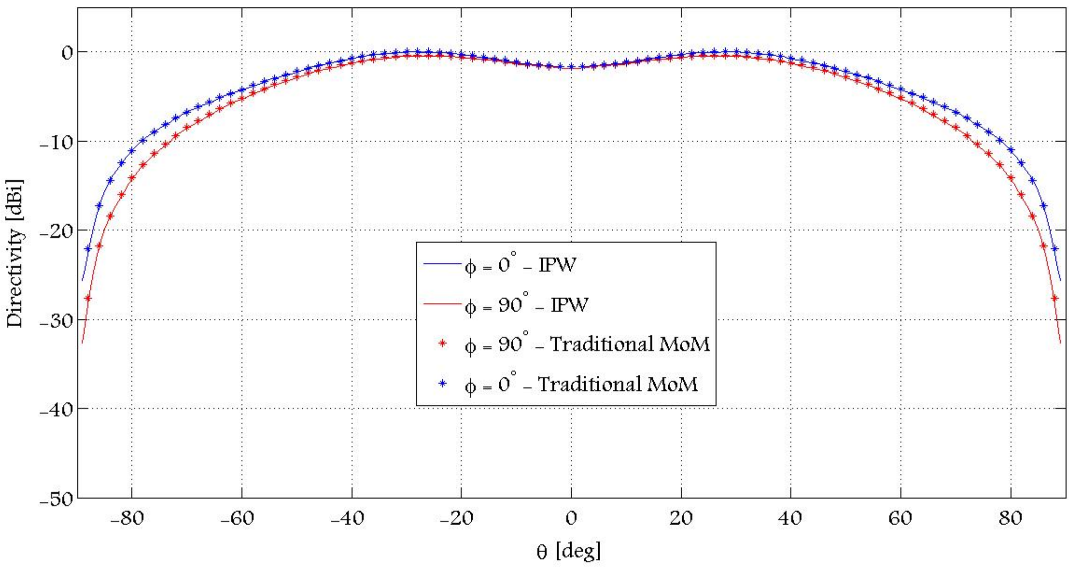

Figure 5.2: Ground radiation pattern with a x-oriented basis function source

5.2 Validation using a patch antenna

In this section, the method is validated with something more consistent than just a basis function. Let us consider a patch antenna represented with discrete points in Figure 5.3. The antenna is placed 0.5 m above the 6 m diameter finite ground plane.

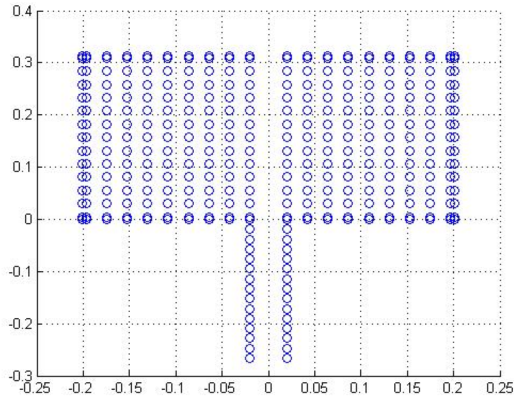

Figure 5.3: Patch antenna

The current on the patch antenna can be modeled using the rooftop basis function described in Chapter 3. The radiation pattern of one of these basis function can be computed similarly to (5.5) except that the result needs to be multiplied by the width of the rectangle.

Performing the same development as the one for the x-oriented basis function except for the radiation patterns of the basis functions, we obtain the results depicted in Figure 5.4. The two solutions overlap quite well once again.

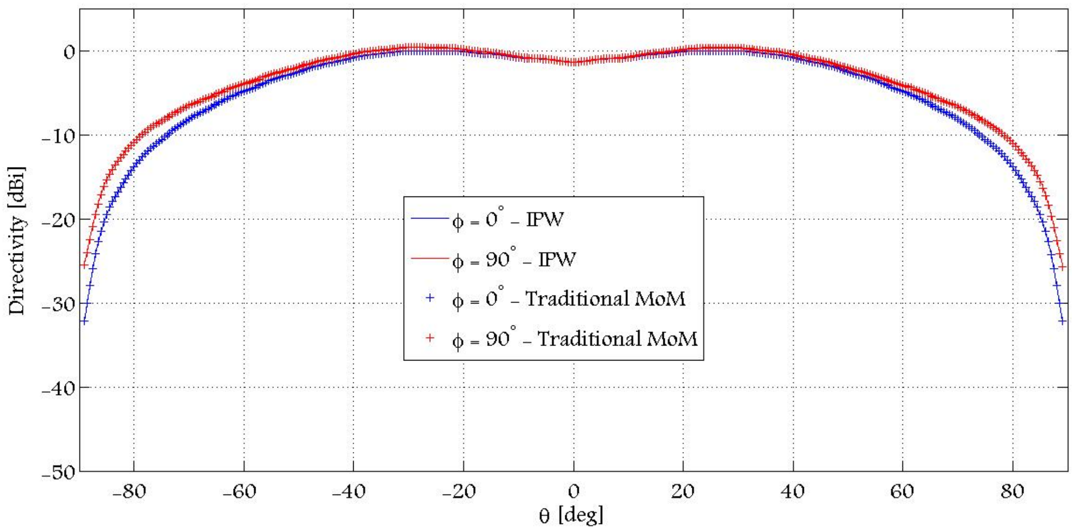

Figure 5.4: Ground radiation pattern with a patch antenna source

5.3 Conclusion

At this stage, we have all the tools necessary to compute the current induced in the finite ground plane and we have ensured that the methods are consistent.

The methodology can now be applied on the SKALA antenna.

Chapter 6

Radiation pattern of the SKALA antenna

This chapter is dedicated to the computation of the whole SKALA antenna radiation pattern in presence of a 6m diameter circular finite ground plane. In the previous chapters, the methods leading to the calculation of the finite ground plane radiation pattern have been described and can now be applied to the SKALA antenna depicted in Figure 6.1.

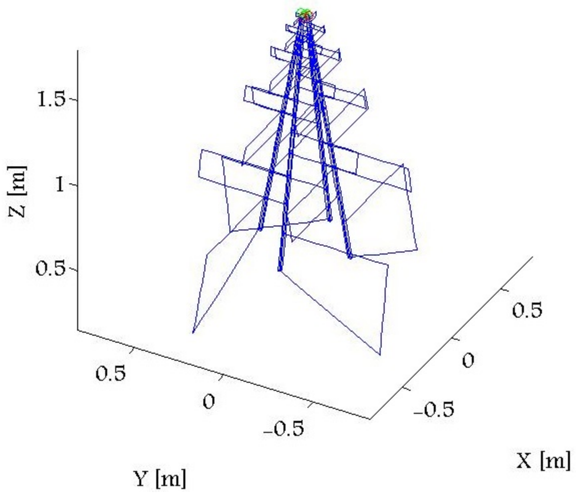

Figure 6.1: SKALA antenna.

This chapter is first devoted to the radiation pattern of the antenna above a ground plane carrying no sources. The radiation pattern of the ground carrying the induced current is then considered. After that, the radiation pattern of the antenna in the vicinity of the finite ground plane carrying the induced current is studied and validated with the software FEKO. The impact of the diameter of the ground is then discussed. Finally, the end of the chapter is devoted to the limitations of the method and the suggested improvements.

6.1 Radiation pattern of the antenna

In the case of the antenna radiation pattern above a ground plane, two kinds of plane waves need to be taken into account:

1. The waves propagating directly above the antenna.
2. The waves reflected on the ground plane.

Considering first the waves propagating above the antenna and using the Far Field approximation, the radiation pattern due to the current on one of the antenna wires can be estimated as follows:

$$
\begin{aligned}
F_{TE} &= \int \left([(-\overrightarrow{J}(\overrightarrow{r'}) \cdot \hat{u}^{+})\hat{u}^{+} + \overrightarrow{J}(\overrightarrow{r'})] \cdot \hat{e}_{te} \right) e^{jkr'\hat{u}^{+}} dL \quad \hat{e}_{te} \\
F_{TM} &= \int \left([(-\overrightarrow{J}(\overrightarrow{r'}) \cdot \hat{u}^{+})\hat{u}^{+} + \overrightarrow{J}(\overrightarrow{r'})] \cdot \hat{e}_{tm} \right) e^{jkr'\hat{u}^{+}} dL \quad \hat{e}_{tm}
\end{aligned}
\tag{6.1}
$$

where $\overrightarrow{J}$ is the current carried by the wire of length L and where $\hat{u}^{+} = \frac{(k_x, k_y, k_z)}{k}$ is the normalized direction of propagation.

The direction of propagation $\hat{u}^{+}$ is considered here for plane waves described by:

$$
\begin{aligned}
k_x &= k \; sin(\theta) cos(\phi) \\
k_y &= k \; sin(\theta) sin(\phi) \\
k_z &= k \; cos(\theta)
\end{aligned}
\tag{6.2}
$$

with k, the wavenumber, $\theta \in [0, \frac{\pi}{2}]$ the elevation angle and $\phi \in [0, 2\pi]$ the azimuth angle.

Gathering all the currents on the antenna and performing the equations (6.1) for each of them using the HARP code, the radiation pattern of the antenna in free space can be calculated. The result, considering a 110 MHz frequency, is depicted in Figure 6.2. The plane characterized by $\phi = 0°$ is aligned with the dipole exciting the antenna on top of it.

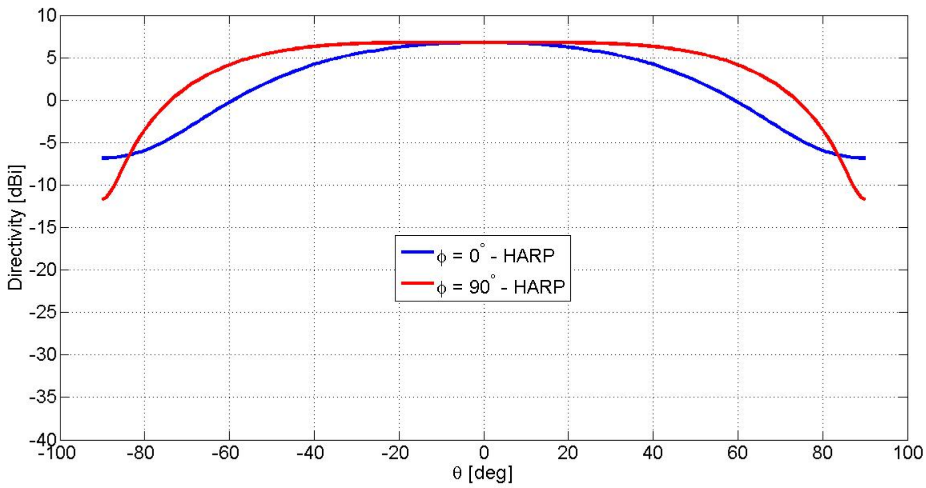

Figure 6.2: Radiation Pattern of the antenna in free space

As mentioned before, the waves reflected by the ground need to be taken into account. A way to account for the reflected waves is to calculate the reflection under the assumption of an infinite ground plane.
The radiation pattern induced from the reflected plane waves in Far Field can be expressed as:

$$
\begin{aligned}
F_{TE} &= \Gamma_{TE}(\hat{u}^{-}) \int \left([(-\overrightarrow{J}(\overrightarrow{r'}) \cdot \hat{u}^{-})\hat{u}^{-} + \overrightarrow{J}(\overrightarrow{r'})] \cdot \hat{e}_{te} \right) e^{jkr'\hat{u}^{-}} dL \quad \hat{e}_{te} \\
F_{TM} &= \Gamma_{TM}(\hat{u}^{-}) \int \left([(-\overrightarrow{J}(\overrightarrow{r'}) \cdot \hat{u}^{-})\hat{u}^{-} + \overrightarrow{J}(\overrightarrow{r'})] \cdot \hat{e}_{tm} \right) e^{jkr'\hat{u}^{-}} dL \quad \hat{e}_{tm}
\end{aligned}
\tag{6.3}
$$

where the expression of the reflection coefficients $\Gamma_{TE}(\hat{u}^{-}), \Gamma_{TM}(\hat{u}^{-})$ is given in Chapter 2 . The direction of the propagation vector now reads: $\hat{u}^{-} = \frac{(k_x, k_y, -k_z)}{k}$ considering the same azimuth and elevation angles as in equation (6.2).

The radiation pattern from direct and reflected plane waves can now be added. The Figure 6.3 depicts the resulting radiation pattern at a frequeny of 110 MHz and compares it to the one obtained with the EM simulation software FEKO.

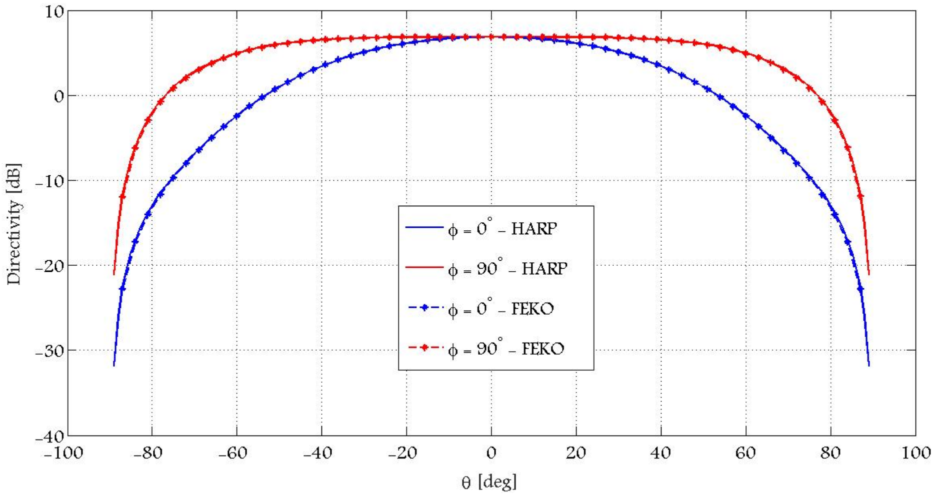

Figure 6.3: Radiation pattern of the antenna above an infinite ground and validation with FEKO

The resulting radiation pattern overlaps quite well with the one from FEKO and thus proofs its consistency. The radiation pattern can be calculated in 15 seconds with the HARP code using MATLAB with an Intel i5 Core processor.

6.2 Radiation pattern of the finite ground plane

The SKALA antenna radiation induces currents in the finite ground plane. This section is devoted to the computation of these currents and the resulting radiation pattern of the ground plane.

At first, the field incident to the ground plane needs to be computed. In the HARP code, there are $N_{bf} = 1218$ basis functions on the antenna describing the currents. Following the method described in Chapter 2, the radiation pattern of each one of the basis functions should be calculated.

The total radiation pattern of the antenna is equivalent to the sum of the radiation patterns of all the basis functions weighted by their respective currents. Starting from equation (2.14), the radiation pattern of one basis function can be expressed as:

$$F_p(k_x, k_y) = \int\int\int_V [\overrightarrow{J}(\overrightarrow{r}') \cdot \hat{e}_p] \; exp\left(-j(k_x x' + k_y y' + k_z z')\right) dV \tag{6.4}$$

for polarization p. Considering the integration only along wires, the following equation can be inferred:

$$F_p(k_x, k_y) = \int [\overrightarrow{J}(\overrightarrow{r}') \cdot \hat{e}_p] \; exp\left(-j(k_x x' + k_y y' + k_z z')\right) dL. \tag{6.5}$$

The integral is similar to the one obtained in Chapter 4 for a x-oriented basis function and can be solved in the same way.

Organizing the radiation patterns of all the basis functions as shown below allows to compute them once for any antenna. After that, one only needs to multiply the matrix of radiation patterns by the current vector of a given SKALA antenna. Noting F_{bi} the radiation pattern for the basis function i, we have:

$$\begin{bmatrix} F_{b1} \\ F_{b2} \\ \dots \\ F_{bN_{bf}} \end{bmatrix}. \tag{6.6}$$

This matrix has dimensions $[N_{bf} \times (nk \times nk)]$ when considering a $[nk \times nk]$ table of plane waves.

The total radiation pattern of a given antenna can then be inferred for any SKALA antenna. Defining I_i the current carried by the basis function i and F_{bt} the total radiation pattern, F_{bt} can be obtained by summing and weighting the columns of the radiation pattern matrix as follows:

$$F_{bt} = \begin{bmatrix} I_1 & I_2 & \dots & I_{N_{bf}} \end{bmatrix} \times \begin{bmatrix} F_{b1} \\ F_{b2} \\ \dots \\ F_{bN_{bf}} \end{bmatrix} \tag{6.7}$$

where each plane wave in F_{bt} carries the information of all the basis functions on the antenna. This operation has to be performed for both TE and TM polarizations.

After that, the field incident to the ground on a given point (x, y, z) produces:

$$E_p(x, y, z) = \frac{-jk\eta}{(2\pi)^2} \int\int F_{bt}(k_x, k_y) \frac{exp\left(-j(k_x x + k_y y - k_z z)\right)}{2jk_z}\, dk_x\, dk_y \tag{6.8}$$

for polarization p.

The next step to find the current in the finite ground plane consists in solving the linear Method of Moments system of equations described in Chapter 3.

Starting from equation (3.12), the projection of the incident field on the testing functions reads:

$$v = -\int \overrightarrow{E} \cdot \overrightarrow{J_t} dS \tag{6.9}$$

The ground plane will be described here with $N_{tf} = 1273$ testing functions.

The mesh characterizing the finite ground plane is composed of triangular basis functions. Using the quadratures described in Chapter 4, the function can be integrated on a chosen number of points by testing functions.

One may notice that the testing functions overlap which means that the field in the integral (6.9) should be calculated several times on the same point. A lot of computation time can be saved by keeping the calculated field in memory and use it on the redundant points.

Starting from the current on the antenna, the excitation vector v in equation (6.9) can be found quite rapidly. If a $[nk \times nk]$ table of inhomogeneous plane waves and a 3 points quadrature is considered, the average execution time of Tables 6.1 and 6.2 can be achieved using MATLAB with an Intel i5 Core processor. As a reminder, these execution times are computed considering an antenna carrying $N_{bf} = 1218$ basis functions and a ground plane described with $N_{tf} = 1273$ testing functions.

Table 6.1: Execution time for different number of plane waves nk and a 3 points quadrature.

nk	Execution Time [s]
32	0.9
64	2.2
128	8.14
256	32.4

The performance of Table 6.2 is obtained when considering a 4 points quadrature.

Table 6.2: Execution time for different number of plane waves nk and a 4 points quadrature.

nk	Execution Time [s]
32	1.5
64	4.5
128	16
256	60

The difference of execution times between Tables 6.1 and 6.2 is mainly due to the different configurations of the quadratures. Indeed, when a 3 points quadrature is considered, the points of interest are placed on the edges of the triangles in contrast with the 4 points quadrature (Figure 4.1). Knowing that the testing functions overlap and are also placed one across the other, they share a lot more points in the case of the 3 points quadrature than in the case of the 4 points quadrature.

At this stage, the radiation pattern of the ground plane can be calculated. Considering a $[128 \times 128]$ table of inhomogeneous plane waves and a 3 points quadrature, the radiation pattern of the ground plane at a 110 MHz frequency is depicted in Figure 6.4.

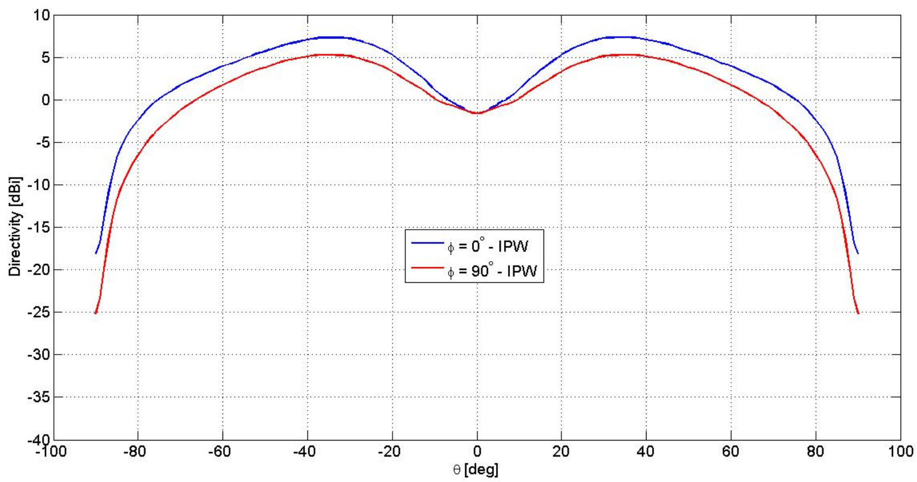

Figure 6.4: Radiation pattern of the ground plane at $f = 110MHz$

6.3 Radiation pattern of the antenna taking into account the finite ground plane

In this section, the contribution of the radiation pattern of the antenna and the finite ground plane are added together and compared to the one obtained with the EM simulation software FEKO.

Using a $[128 \times 128]$ table of inhomogeneous plane waves and a 3 points quadrature, the total radiation patterns considering frequencies of 80 MHz, 110 MHz and 200 MHz are depicted in Figures 6.5 , 6.6 and 6.7. The radiation pattern at a frequency of 350 MHz requires more plane waves, the result using a $[256 \times 256]$ table of plane waves is pictured in Figure 6.8. One can see in Figure B.1 that using a table of $[128 \times 128]$ plane waves in the 350 MHz case is not sufficient.

The comparison with FEKO is quite good at low frequencies, the shift between the two radiation patterns does not exceed 0.5 dB at grazing angles and 0.2 dB for vertical angles. More differences appear when considering the 200 MHz and 350 MHz frequencies. In the case of the 350 MHz simulation, the worst case shift reaches 3 dB for elevation angles around 70°. The shift is globally less pronounced for vertical angles.

The differences between the FEKO curves and the approximations may come from different factors:

- The accuracy of the method of decomposition into inhomogeneous plane waves may decrease when considering larger frequencies.
- The currents on the antenna calculated with the infinite ground plane assumption in the HARP code.
- The thin wire assumption and the modeling of the tubular support represented as a cage made of thin wires with square sections made in the HARP code [17].

The radiation pattern presents more spikes at higher frequencies. These spikes may be due to the higher contribution of the short arms of the SKALA antenna. Indeed, at low frequencies the wavelength is larger and the radiation pattern from the current present in the short arms on top of the antenna do not have a great contribution on the radiation pattern. When we increase the frequency, the wavelength is smaller and the current in the short arms has a greater impact on the total radiation pattern.

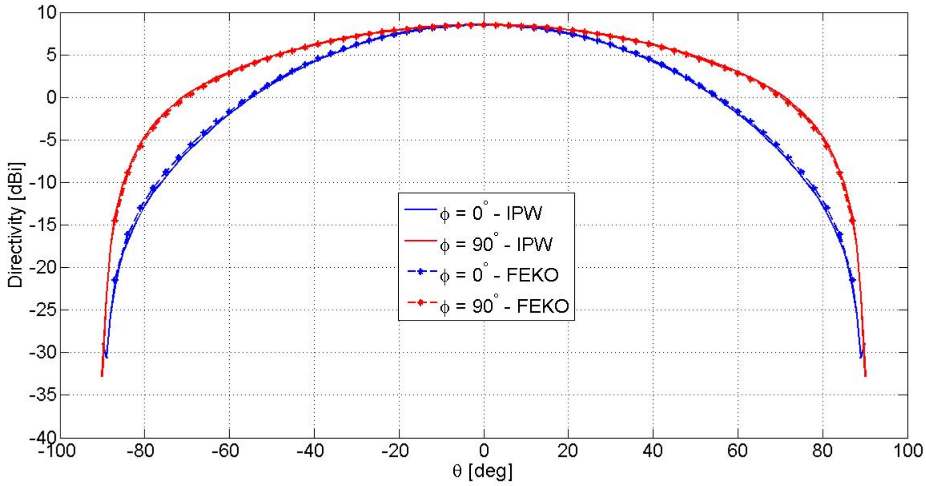

Figure 6.5: Total radiation pattern at $f = 80\ MHz$ and comparison with FEKO

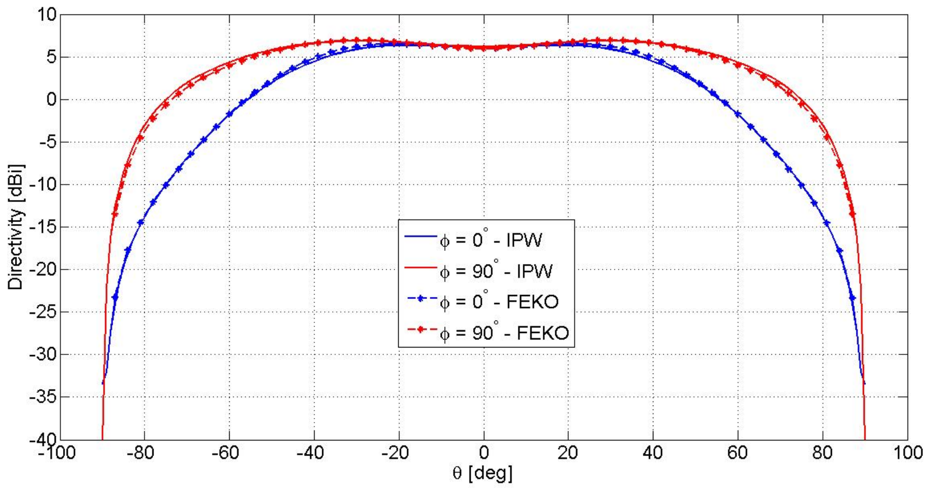

Figure 6.6: Total radiation pattern at $f = 110\ MHz$ and comparison with FEKO

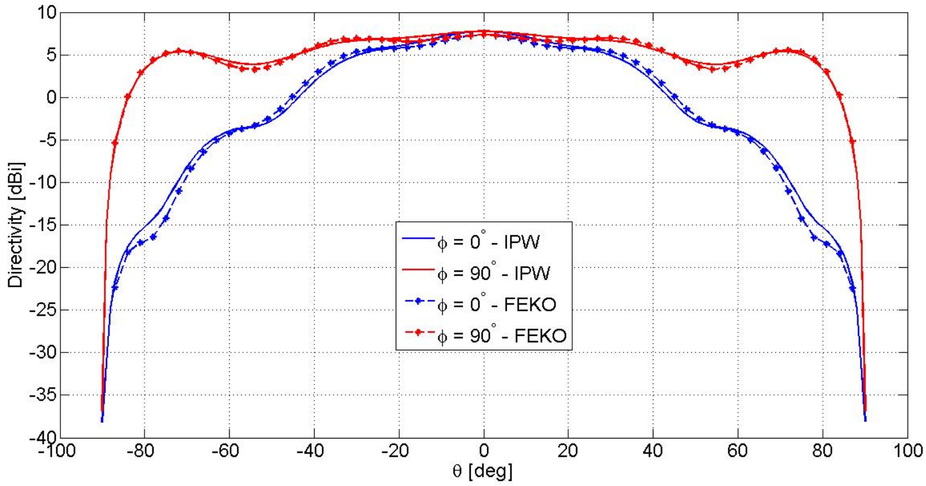

Figure 6.7: Total radiation pattern at $f = 200\ MHz$ and comparison with FEKO

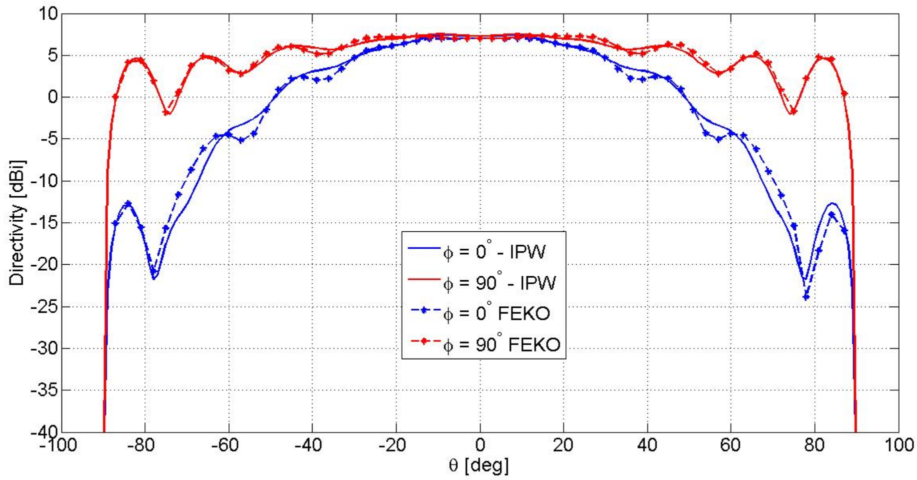

Figure 6.8: Total radiation pattern at $f = 350\ MHz$ and comparison with FEKO

6.4 Influence of the ground

In this section, the influence of the finite ground plane is more precisely discussed. The total radiation pattern has been computed considering a ground diameter of 8 m instead of 6 m. The results are depicted and compared to those of FEKO for different frequencies in Figures B.2, B.3 and B.4. We chose to have about the same number of testing functions on the 8 m diameter ground and on the 6 m diameter ground plane. It means that the triangles composing the mesh in the 8 m diameter ground are bigger than in the 6 m diameter ground. The integration using quadrature is then less accurate and we need a 4 point quadrature instead of 3 to have acceptable results. The execution time is then impacted by the increase of the ground plane diameter.

Let us first consider the radiation pattern of the ground plane at a frequency of $110MHz$. There is a strong difference when considering a diameter of 8 m instead of 6 m as one can see in Figure 6.9.

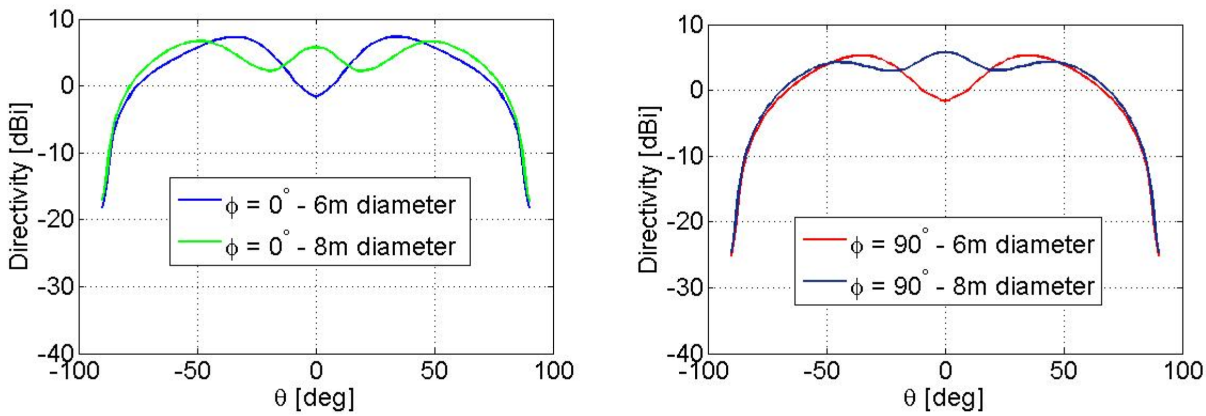

Figure 6.9: Radiation pattern of the ground plane considering 6 m and 8 m diameters.

An analogy can be established between the finite ground plane and concentric circles of antennas. Let us consider small antennas in place of the testing functions. We can assume that the amplitudes of all the antennas placed on the same circle are quite constant thanks to the symmetry of the SKALA antenna. From there, increasing the size of the circular ground plane is equivalent to add concentric circles containing antennas with different amplitudes changing then the radiation pattern of the system.

One can see the impact of the 6 m and 8 m diameter ground planes on the radiation pattern of the antenna in Figure 6.10 for azimuth angle $\phi = 90°$. The red curve represents the radiation pattern of the antenna above an infinite ground plane carrying no sources. The green and blue curves represent the total radiation pattern taking into account the 6 m and 8 m diameter ground planes. The radiation pattern is significantly influenced by the finite ground plane for elevation angles $|\theta| < 50°$, it can be less or more intense in this region depending on the ground plane diameter. However, the total radiation pattern is decreased for angles $|\theta| > 50°$.

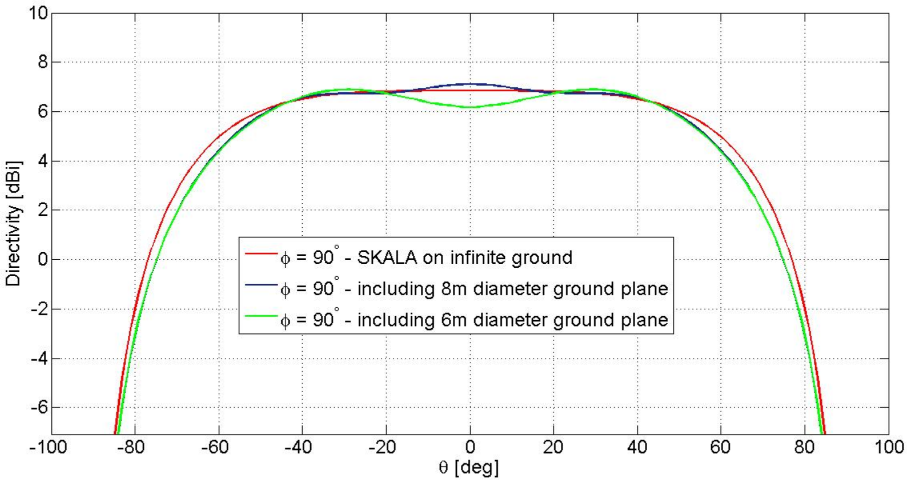

Figure 6.10: Radiation pattern of the antenna alone above the infinite ground and total radiation pattern when including the ground plane

6.5 Limitations and suggested improvements

The speed of the method directly depends on the number of plane waves considered. It appears that using a table of $[32 \times 32]$ plane waves instead of $[128 \times 128]$ gives the same result at 110 MHz for the 6 m diameter ground plane. Referring to the execution times of Table 6.1, the induced current can be estimated in less than one second. However, the increase of the frequency means a higher number of plane waves and the execution time grows considerably. At 350 MHz, we need a table of $[256 \times 256]$ plane waves which leads to an execution time above 30 seconds. When considering tables of hundreds of SKALA antennas, these changes of execution time may become important.

In this project, the currents on the antenna have been calculated under the assumption of an infinite ground plane. We could achieve improvements by calculating the current on the antenna and on the finite ground plane with an iterative method. The main idea is to solve iteratively the following matrix system:

$$Z\ x = b \tag{6.10}$$

with x composed of the excitation vectors of both the antenna and the ground plane, b the current induced and Z the matrix composed of the impedance matrix of the antenna, the impedance matrix of the ground and the two matrices corresponding to the mutual impedances between the ground and the antenna.

The Z matrix has the following form:

$$\begin{bmatrix} Z_{11} & Z_{12} \\ Z_{21} & Z_{22} \end{bmatrix} \tag{6.11}$$

where Z_{11} is the impedance matrix of the antenna, Z_{22} is the impedance matrix of the ground plane and Z_{12}, Z_{21} are the mutual impedances between the antenna and the ground plane.

The Z_{12} matrix can be obtained by a matrix multiplication of the radiation pattern matrices of the antenna and the ground plane. Let us call A the matrix composed of the radiation patterns of the basis functions of the antenna. A corresponds to the matrix shown in (6.6). Another matrix corresponding to the radiation patterns of the testing functions placed on the ground plane can be defined as B. The mutual impedance matrix Z_{12} can be calculated as: $Z_{12} = A * B$. After that, Z_{21} is found by transposing the matrix Z_{12}.
The system in equation (6.10) could be solved using the Krylov method [19].

6.6 About the software FEKO

This section gives some characteristics of the EM simulation software FEKO [18].

FEKO is based on the Method of Moments and was the first software to use the multi-level fast multipole method (MLFMM) to solve electrically large problems. The MLFMM is based on the Method of Moments but allows lower memory requirements.
The Method of Moments in FEKO is hybridized with the following techniques:

- Finite Element Method.
- Physical Optics.
- Ray-launching Geometric Optics.
- Uniform Theory of Diffraction.

Chapter 7

Conclusion

From the method of decomposition into inhomogeneous plane waves to the Gaussian quadratures, a method to compute relatively rapidly the current induced in a finite ground plane placed under a given source has been built.

The method was tested, then applied to the SKALA antenna and the results were validated against the EM simulation software FEKO. This method can be adapted to changes of frequency and of ground plane diameter. However, when considering the high frequencies of the SKALA antenna (350 MHz for example), the method can be accurate but may need more execution time.

Furthermore, there is still a lot of place for research in this field. The method has to be applied in a relevant environment, not only for one SKALA antenna, but for a table of hundreds of antennas composing the Low Frequency Array Aperture of the SKA.

Appendix A

Calculation of the reflection coefficients

The boundary conditions read:

$$\begin{aligned} \hat{z} \times E^u &= \hat{z} \times E^d \\ \hat{z} \times H^u &= \hat{z} \times H^d. \end{aligned} \tag{A.1}$$

Starting with a wave coming from the upper medium and considering first the TE case, the first equation in $(A.1)$ gives:

$$\hat{z} \times \left(-\hat{m}E_{TE}^i - \hat{m}E_{TE}^r\right) = \hat{z} \times -\hat{m}E_{TE}^d \tag{A.2}$$

where E_{TE}^i and E_{TE}^r are the TE amplitudes of the incident and reflected waves. The polarization vector in the interface needs to be the same in the two sides of the equation.

From there, the following equation can be inferred:

$$E_{TE}^i + E_{TE}^r = E_{TE}^d. \tag{A.3}$$

From the second equation in $(A.1)$, we have:

$$\frac{1}{\eta_1}\hat{z} \times \left(\hat{e}^{u-}E_{TE}^i + \hat{e}^{u+}E_{TE}^r\right) = \frac{1}{\eta_2}\hat{z} \times \hat{e}^{d-}E_{TE}^d. \tag{A.4}$$

Using the fact that $\hat{z} \times \hat{e}^{u-} = -\hat{z} \times \hat{e}^{u+}$,

$$\frac{1}{\eta_1}\hat{z} \times \hat{e}^{u-}\left(E_{TE}^i - E_{TE}^r\right) = \frac{1}{\eta_2}\hat{z} \times \hat{e}^{d-}E_{TE}^d. \tag{A.5}$$

Considering $(A.3)$,

$$\frac{1}{\eta_1}\hat{z} \times \hat{e}^{u-}\left(E_{TE}^i - E_{TE}^r\right) = \frac{1}{\eta_2}\hat{z} \times \hat{e}^{d-}\left(E_{TE}^i + E_{TE}^r\right). \tag{A.6}$$

Using (2.39) and (2.42),

$$\frac{\eta_2}{\eta_1}\frac{ct_u}{ct_d}\left(\Gamma_{TE}^u - 1\right) = \Gamma_{TE}^u + 1, \tag{A.7}$$

$$\Gamma_{TE}^u = \frac{ct_u\eta_d + ct_d\eta_u}{ct_u\eta_d - ct_d\eta_u}. \tag{A.8}$$

For the TM case, the first equation in $(A.1)$ gives:

$$\hat{z} \times \left(\hat{e}^{u-}E_{TM}^i + \hat{e}^{u+}E_{TM}^r\right) = \hat{z} \times \hat{e}^{u-}E_{TM}^d, \tag{A.9}$$

leading to

$$\frac{ct_u}{ct_d}\left(E^i_{TM} - E^r_{TM}\right) = E^d_{TM}. \tag{A.10}$$

Given the second equation in $(A.1)$ for the TM case,

$$\frac{1}{\eta_1}\hat{z} \times \left(\hat{m}E^i_{TM} + \hat{m}E^r_{TM}\right) = \frac{1}{\eta_2}\hat{z} \times \hat{m}E^d_{TM}. \tag{A.11}$$

Using $(A.10)$,(2.39) and (2.42) :

$$\frac{\eta_2}{\eta_1}\frac{ct_d}{ct_u}\left(\Gamma^u_{TM} + 1\right) = \Gamma^u_{TM} - 1 \tag{A.12}$$

which finally leads to:

$$\Gamma^u_{TM} = \frac{ct_u\eta_u + ct_d\eta_d}{ct_u\eta_u - ct_d\eta_d}. \tag{A.13}$$

Appendix B

Different radiation patterns

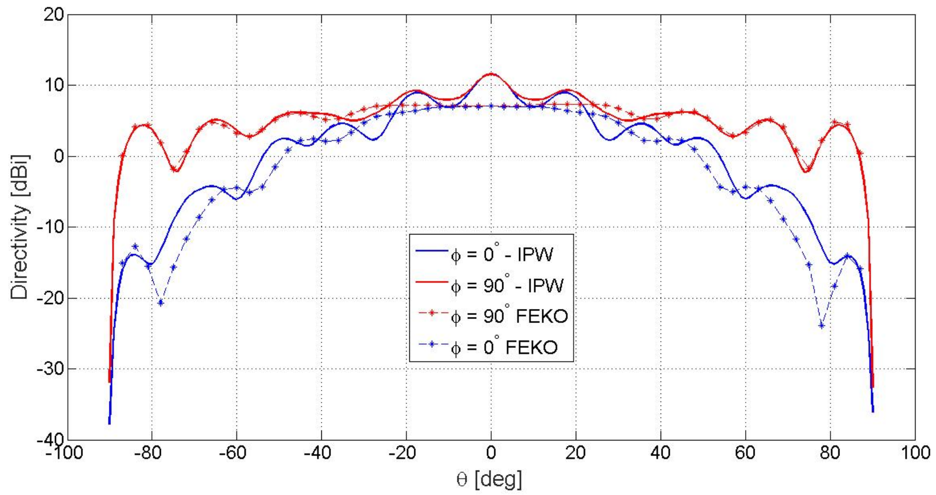

Figure B.1: Total radiation pattern at $f = 350\ MHz$ for a 6 m diameter ground with $nk = 128$

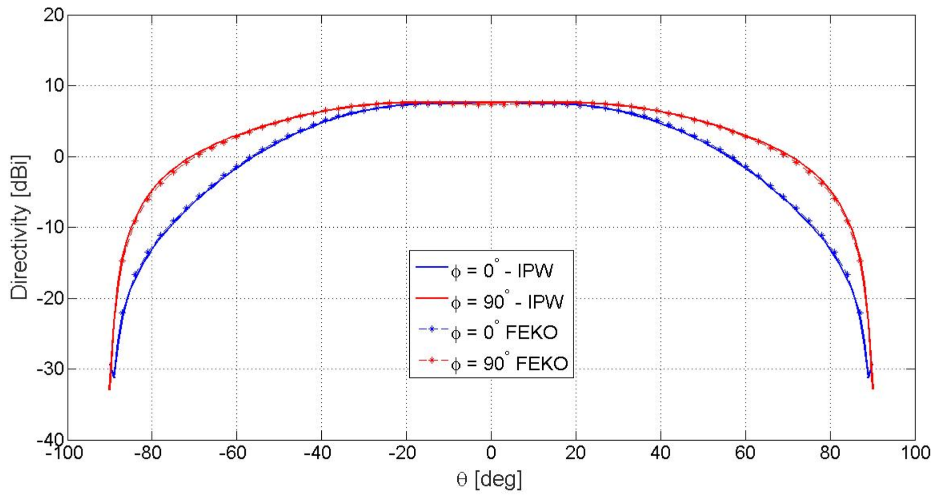

Figure B.2: Total radiation pattern at $f = 80\ MHz$ for a 8 m diameter ground with $nk = 64$ and comparison with FEKO

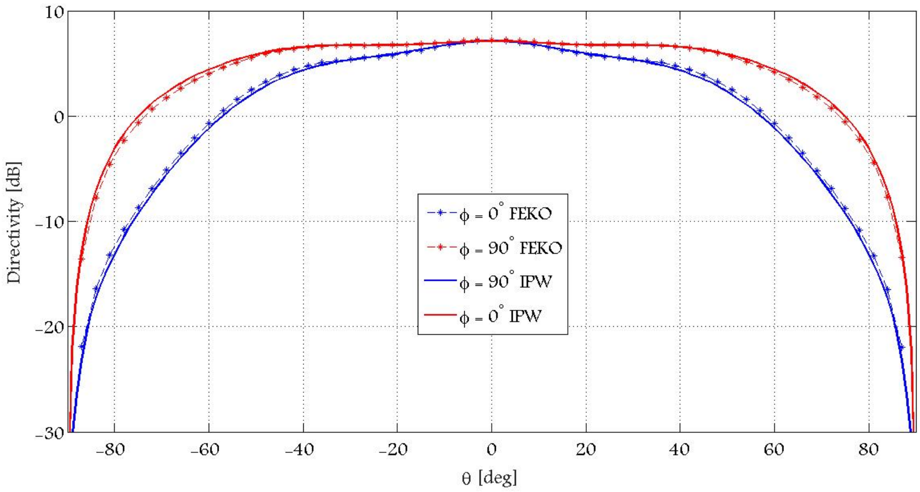

Figure B.3: Total radiation pattern at $f = 100\ MHz$ for a 8 m diameter ground with $nk = 64$ and comparison with FEKO

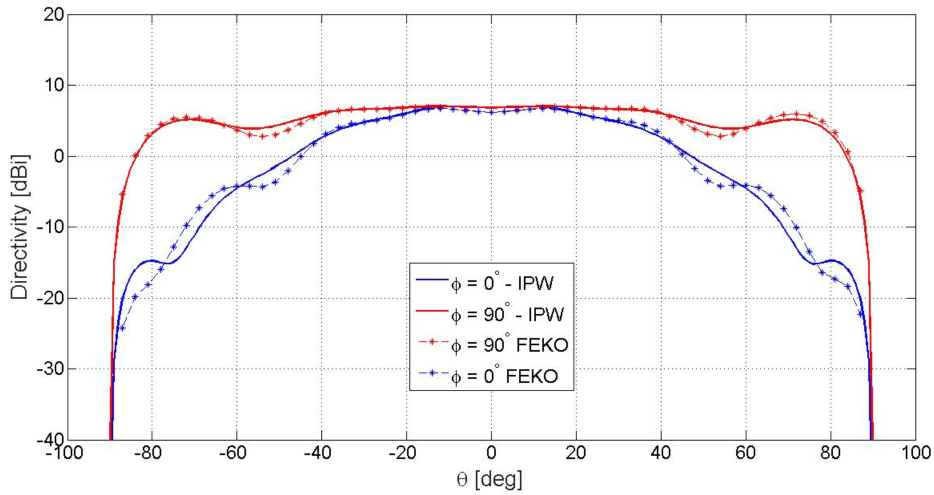

Figure B.4: Total radiation pattern at $f = 200\ MHz$ for a 8 m diameter ground with $nk = 64$ and comparison with FEKO

Bibliography

[1] www.skatelescope.org

[2] E. de Lera Acedo et al., "SKALA, a log-periodic array antenna for the SKA-low instrument: design, simulation, tests and system considerations," *in Proc. International Conference on Electromagnetics in Advanced Applications (ICEAA)*, 2012.

[3] Ha Bui Van, Jens Abraham, Quentin Gueuning,Eloy de Lera Acedo, Christophe Craeye, "Further Validation of Fast Simulation Method at The Element and Array Pattern Levels for SKA," *in Proc. Eucap Conf.*, April 2016.

[4] Khaldoun Alkhalifeh, Greg Hislop, Nilufer A. Ozdemir, Christophe Craeye , "Efficient MoM Simulation of 3D Antennas in the vincinity of the ground," *IEEE Transactions on Antennas and Propagation.*

[5] Weyl, H. "Ausbreitung elektromagnetische Wellen ber einem ebenen Leiter." Annalen der Physik 365: pp. 481-500, 1919.

[6] Shambhu Nath Jha,Christophe Craeye , "Contour-FFT Based Spectral Domain MBF Analysis of Large Printed Antenna Arrays," *IEEE Transactions on Antennas and Propagation, Nov. 2014*

[7] Balanis Constantine A., *Antenna Theory*, pp. 151-154, 1st ed. Hoboken, New Jersey: John Wiley & Sons, 2005.

[8] E. Martini, C. Craeye, N. Ozdemir and S. Maci, "Harmonics-based inhomogeneous plane-wave method (HIPW)," IEEE Trans. Antennas Propag., May 2015.

[9] C. Craeye, "Slides : LELEC2910 "

[10] Simon Hubert and Christophe Craeye , "Notes: Planar Green's Functions," November 2016.

[11] Shambhu Nath JHA, "Fast Spectral-Domain Macro Basis Function Analysis of Large Arrays of Printed Antennas," June 2014.

[12] Xavier Dardenne, "Method of Moments Simulations on Infinite and Finite Periodic Structures and Application to High-Gain Metamaterial Antennas," March 2007.

[13] C. Geuzaine and J-F. Remacle, "Gmsh: a three dimensional finite element mesh generator with built in pre and post processing facilities," *http://geuz.org/gmsh/*

[14] R.F. Harrington, "Field Computations by Moment Method in Electromagnetics," Krieger, Malabar, Fla., 1982.

[15] http://math2.uncc.edu/ shaodeng/TEACHING/math5172/Lectures/Lect_15.PDF

[16] S.M. Rao, D.R.Wilton, and A.W. Glisson, "Electromagnetic scattering by surfaces of arbitrary shape," *IEEE Transactions on Antennas Propagation*, vol. 30, pp. 409-418, 1982.

[17] Q. Queuning, C. Raucy,C. Craeye, E. Colin-Beltran, E. de Lera Acedo, "Mutual coupling analysis in non-regular arrays of SKALA antennas with the HARP approach," AP-S, 2015.

[18] www.feko.info

[19] Y. Saad and M. H. Schultz, “GMRES: A Generalized Minimal Residual Algorithm for Solving Nonsymmetric Linear Systems,” SIAM Journal on Scientific and Statistical Computing, vol. 7, no. 3, pp. 856–869, 1986.

Rue Archimède, 1 bte L6.11.01, 1348 Louvain-la-Neuve www.uclouvain.be/epl